PNAS

Supporting Information for

A Tale of Two Topological Isomers: Uptuning $[Fe^{IV}(O)(Me_4cyclam)]^{2+}$ for Olefin Epoxidation

Bittu Chandra[1], Faiza Ahsan[2], Yuan Sheng[1], Marcel Swart,[2,3]* and Lawrence Que, Jr.[1]*

[1]Department of Chemistry, University of Minnesota, Minneapolis, Minnesota 55455, United States

[2]IQCC and Department of Chemistry, University of Girona, 17003 Girona, Spain

[3]ICREA, 08010 Barcelona, Spain

ORCIDs: 0000-0001-6071-8071 (BC), 0000-0003-4694-6515 (FA), 0 000-0003-0098-7100 (YS), 0000-0002-8174-8488 (MS), 0000-0002-0989-2813 (LQ)

Corresponding author names: Marcel Swart, Lawrence Que, Jr.
Email: marcel.swart@gmail.com, larryque@umn.edu

This PDF file includes:

Table of Contents

Experimental Section:

Materials and Instrumentation

All chemicals and solvents were of commercially available quality and used without further purification unless otherwise specified. The reagents iodosylbenzene (PhIO) and 2-(tert-butylsulfonyl)iodosylbenzene (*s*-ArIO, soluble version of PhIO) were synthesized according to previously published procedures (1). All moisture and oxygen sensitive compounds were synthesized in a nitrogen-filled glove box. $Fe^{II}(OTf)_2 \bullet 2CH_3CN$ (2) and $[Fe^{II}(TMC)(OTf)](OTf)$ (3) were prepared according to the published procedures. Oxoiron(IV) complexes, *anti*-$[Fe^{IV}(O)(TMC)(CH_3CN)]^{2+}$ and *syn*-$[Fe^{IV}(O)(TMC)(CH_3CN)]^{2+}$ isomers were synthesized according to previously published reports (3, 4).

UV-Vis absorption spectra were recorded on an HP8453A diode array spectrometer equipped with a cryostat from Unisoku Scientific Instruments (Osaka, Japan). The same instrument was used for UV-Vis kinetics experiments. NMR spectra were recorded in deuterated solvents using a Bruker 400 or 500 MHz spectrometer at 298 K. GC-MS measurements were performed on an AGILENT 7200 QTOF-MS spectrometer. This Agilent 7200 GC/QTOF-MS is a directly combined gas chromatograph-quadrupole time-of-flight mass spectrometer for accurate mass GC/MS and GC/MS/MS measurements.

[*Caution*: The synthesis of 2-(tert-butylsulfonyl)iodosylbenzene has recently led to an injury of a researcher. Appropriate safety measures should be taken.]

Generation of *anti*-$[Fe^{IV}(O)(TMC)(CH_3CN)]^{2+}$ (TMC-*anti*).

Complex $Fe^{II}(TMC)(OTf)_2$ (61 mg, 0.1 mole) was dissolved in a CD_3CN (3 mL)/trifluoroethanol (TFE) (3 mL) solvent mixture, to which solution PhIO (22 mg, 0.1 mole) powder was added in one portion. The slurry was allowed to stir for 2 min (becoming clear after 1 min) before the addition of 25 mL Et_2O for its precipitation. The precipitants were collected, washed with Et_2O, and dried in vacuo to be directly used as TMC-*anti*.

For UV-Vis kinetics experiments, 1.0 mM TMC-*anti* solutions were generated in situ from a stock solution of $Fe^{II}(TMC)(OTf)_2$ (10 mM in CH_3CN) in 1.0 mL CH_3CN using 1.5 mM of PhIO (100 mM solution in trifluoroethanol).

Generation of *syn*-$[Fe^{IV}(O)(TMC)(CH_3CN)]^{2+}$ (TMC-*syn*).

Complex $Fe^{II}(TMC)(OTf)_2$ (6.1 mg, 0.01 mole) was dissolved in CD_3CN (1 mL) under an inert atmosphere (N_2) followed by the addition of 1 equiv. of 2-^{t}BuSO$_2$-C_6H_4IO (*s*-ArIO) (3.4 mg, 0.01 mmol), dissolved in anhydrous trifluoroethanol (50 μL), at room temperature. TMC-*syn* was generated instantly upon mixing.

For UV-Vis kinetics experiments, 1.0 mM TMC-*syn* was generated in situ from a stock solution of $Fe^{II}(TMC)(OTf)_2$ (10 mM in CH_3CN) in 1.0 mL CH_3CN using 1.1 mM of *s*-ArIO (100mM solution in trifluoroethanol/dichloromethane).

Substrate oxidation kinetics and product analysis

Kinetic measurements of substrate oxidations were performed at 25 °C under N_2 atmosphere. 1.0 mM TMC-*anti* and TMC-*syn* complexes were first generated in 1 mL MeCN solution using ~1.5 equivalents of PhIO and *s*-ArIO respectively, followed by the addition of various concentrations of substrate. The decay of the associated 825-nm (for TMC-*anti*) or 815-nm (for TMC-*syn*) UV-Vis bands was then monitored over time. Fitting the decay of TMC-*anti/syn* to a single-exponential function yielded a pseudo-first-order rate constant, k_{obs}. Second-order rate constants, k_2 ($M^{-1}s^{-1}$), were determined from the slopes of plots of k_{obs} (s^{-1}) versus substrate concentration.

To isolate and identify the organic products upon completion of the reaction, the reaction mixtures were filtered through a plug of silica and eluted with chloroform or ethyl acetate. The filtered solutions were then analyzed by GC/GC-MS with naphthalene as the quantification standard. Alternatively, the mixtures may also be worked up according to published methods involving the treatment of the reaction solution with dilute acid.

Theoretical Section:

Computational details

All DFT calculations were performed with the Amsterdam Density Functional (ADF) (5, 6), and QUILD (7) programs. Molecular orbitals were expanded in an uncontracted set of Slater-type orbitals (STOs) of triple-ζ quality with double polarization functions (TZ2P) (8, 9). Core electrons were not treated explicitly during the geometry optimizations (frozen core approximation[6]). An auxiliary set of s, p, d, f, and g STOs was used to fit the molecular density and to represent the Coulomb and exchange potentials accurately for each SCF cycle.

Geometries of all possible spin states were optimized with the QUILD (7) program using adapted delocalized coordinates until the maximum gradient component was less than 10^{-4} a.u. Energies, gradients, Hessians (10) (for vibrational frequencies), and UV-vis spectra were calculated using B97-D3, (11, 12) in all cases by including solvation effects through the COSMO (13) dielectric continuum model with appropriate parameters for the solvents (14). For computing Gibbs free energies, all small frequencies were raised to 100 cm^{-1} in order to compensate for the breakdown of the harmonic oscillator model (15, 16). Scalar relativistic corrections have been included self-consistently in all calculations (except the Mössbauer calculations) by using the zeroth-order regular approximation (ZORA) (17). Most B97D3 calculations were performed with a Becke grid of Normal quality. All DFT calculations were performed using the unrestricted Kohn-Sham scheme.
All computational data have been uploaded onto the IOCHEM-BD platform (www.iochem-bd.org), DOI: https://doi.org/10.19061/iochem-bd-4-65, to facilitate data exchange and dissemination, according to the FAIR principles (18) of OpenData sharing.

Minimum Energy Crossing Point (MECP)

The minimum energy crossing point (MECP) is that point in space where the energy surfaces of two spin states cross (see below the MECP is similar to conical intersections (19-21), with similar strategies for structure determination. Instead of

normal geometry optimizations where the curvature of the Hessian (2nd derivative of energy w.r.t. atomic coordinates) should be all positive, or transition-state searches where one normal coordinate should be maximized and all others minimized, in the case of MECP the mathematical formulation is a bit more complex because: (i) it involves two energy surfaces, and (ii) there is the constrained search such that the energy of surface A matches the energy of surface B; at the same time, all other coordinates should be minimized. Harvey and coworkers (22) were among the first to provide a computer program to handle this. Based on many reports in the literature (23, 24), it was observed that the energy needed to reach the MECP is of the order of 5-10 kcal·mol^{-1}, which is usually lower than the barriers for the chemical reactions. Hence, usually one can assume that the spin-state crossing through the MECP is sufficiently fast in comparison to the chemical reaction, and will not hinder the reaction mechanism.

Definition of the out-of-plane distances for Fe (Fe-oop), O (O-oop), and CH_3CN-N (N-oop)

The four equatorial nitrogens of the TMC ligand are chosen, the corresponding center of mass (com-N) is computed, and then the principal moments of the inertia tensor are computed with respect to this center of mass. The latter is diagonalized, which defines the X, Y, and Z vectors for the plane that goes through the four nitrogens. Then, the coordinates of the whole complex (global XYZ coordinates) are transformed such that the center of the axis system coincides with com-N, and the axes lie along the above-mentioned X, Y, and Z vectors (local coordinate system).

As an example, shown here are the coordinates of the four nitrogens at the TS of the HAT reaction with DHA and TMC-*syn* (*S* = 2):

N	1.03995612	-1.83540142	0.87437296
N	1.93136180	-1.25473012	-1.85745010
N	1.78697439	2.04010895	-1.13897969
N	0.89994963	1.36091269	1.56910570

with com-N:

Center of mass 1.41456048 0.07772253 -0.13823778

The (3x3) inertia tensor is as follows:

263.754403 -1.380048 35.284660
-1.380048 121.977433 -8.131214
35.284660 -8.131214 164.493834

After diagonalization, the moments of inertia are obtained:

Moments of inertia 120.26 154.86 275.11

with the following transformation matrix to move from the global XYZ system to the local one:

Transformation matrix

-0.04319472 0.97591404 0.21383640
0.30339551 0.21674152 -0.92788700
-0.95188517 0.02479718 -0.30545002

After transformation to the local XYZ system, the coordinates are as follows:

N	-1.634331	-1.467895	-0.000162
N	-1.690313	1.463232	0.000157
N	1.685039	1.466895	-0.000157
N	1.639604	-1.462232	0.000162
O	-0.003253	0.072048	**1.900970**
Fe	-0.001329	0.044674	**0.218838**
N	-0.000268	0.207523	**-2.040926**

The out-of-plane distance for iron (Fe-oop), oxygen (O-oop), and CH_3CN-N (N-oop) are then simply the corresponding Z-coordinates in the local coordinate system:

O-oop 1.901 Å
Fe-oop 0.219 Å
N-oop -2.041 Å

Spin-resolved charge displacement function (SR-CDF) analysis

As described in *Chem. Commun.* **2020**, *56*, 12146, (25) the charge displacement function analysis is based on a fragment approach, where the flow of electrons within a molecule or transition metal complex is estimated. In particular, how much the charge density changes when the two fragments are brought together to the geometry they obtain in the complex. The charge displacement function, Δq(z), measures at each point z along a chosen axis the amount of electrons that move across a plane perpendicular to this axis passing through z.

$$\Delta q(z) = \int_{-\infty}^{z} dz' \int_{-\infty}^{\infty}\int_{-\infty}^{\infty} \Delta\rho(x,y,z')\, dx\, dy \qquad (1)$$

Typically, the z-axis is chosen to lie along a chemically meaningful bond, which in our case is the Fe=O bond. Positive values of Δq(z) correspond to electrons flowing in the direction of decreasing z, and negative values to electrons moving to increasing z. A positive slope indicates regions of charge accumulation, and vice versa a negative slope indicates depletion (26). Originally, the CDF was applied only to closed-shell systems but in 2020 (25), we investigated its use for open-shell systems.

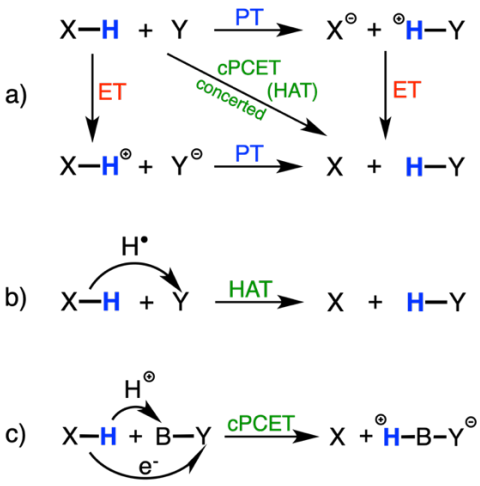

Scheme S1. a) Concerted vs stepwise CPET mechanism. b) Hydrogen atom transfer (HAT). c) Concerted proton-couplet electron transfer (cPCET).

We explored the use of the spin-resolved CDF for distinguishing between Hydrogen Atom Transfer (HAT) and concerted Proton Coupled Electron Transfer (cPCET) (see Scheme S1) for two proto-typical reactions, which Klein and Knizia

had studied by following the intrinsic bond orbitals along the reaction pathway (27). They demonstrated clearly how these orbitals can be followed to see where the electrons are moving to, and as such were able to distinguish between HAT and cPCET. The difference between the two mechanisms is whether the electron and proton are moving to the same place (HAT) or to different places (cPCET).
We were able to show that the SR-CDF at the transition states of these two reactions have distinct profiles:

HAT **cPCET**

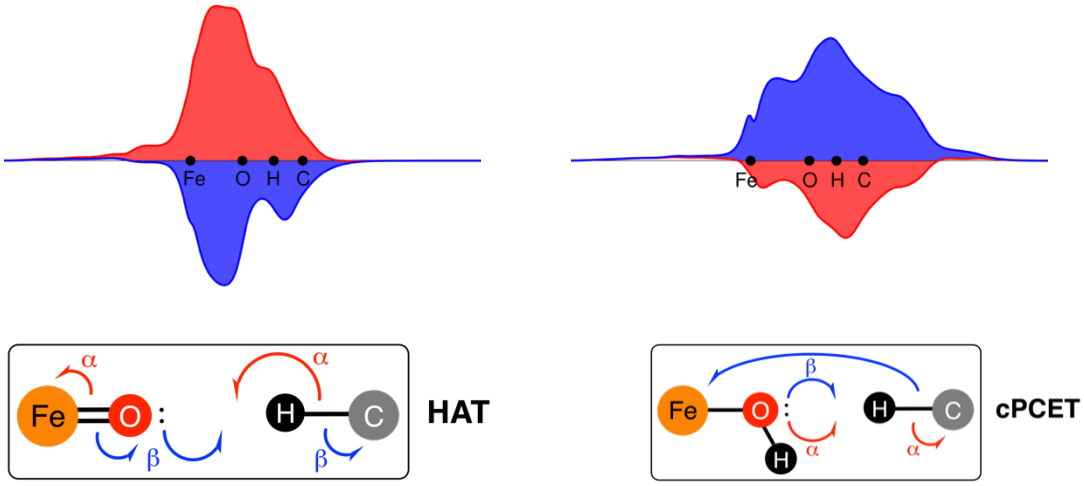

(reproduced with permission from *Chem. Commun.* **2020**, *56*, 12146)

In the HAT mechanism, the alpha-electrons are moving to the left, and the beta-electrons to the right. Vice versa, for cPCET, the beta-electrons are moving to the left, and the alpha-electrons to the right. Note that both were in high-spin S = 2 state, i.e. with four more alpha-electrons than beta-electrons. Interestingly, this flow of electrons follows the arrow pushing as one would normally describe things (*vide supra*).
By applying the same SR-CDF analysis to the HAT reaction with DHA, we observe the same profile in Figure S1 as found in 2020 for HAT mechanism: the alpha electrons are moving to the left, and beta-electrons to the right.

TS_TMC-*anti*_DHA **TS_TMC-*syn*_DHA**

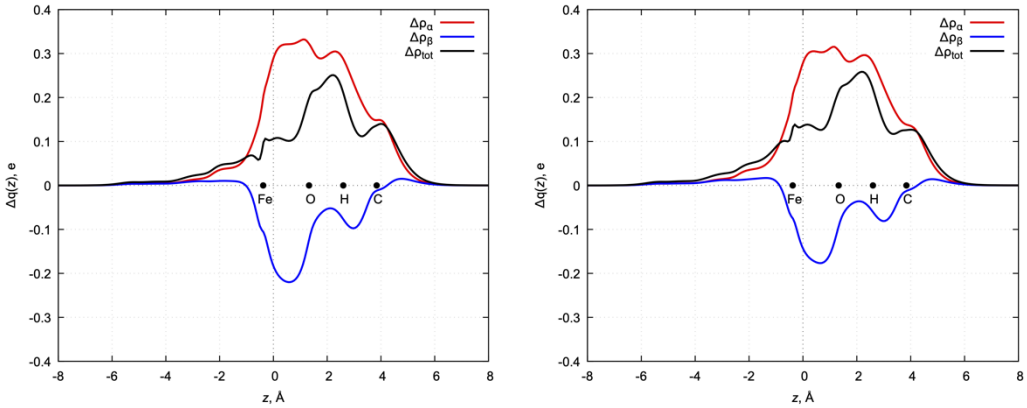

Fig. S1 SR-CDF analysis for HAT reaction of TMC-*anti* and TMC-*syn* with DHA

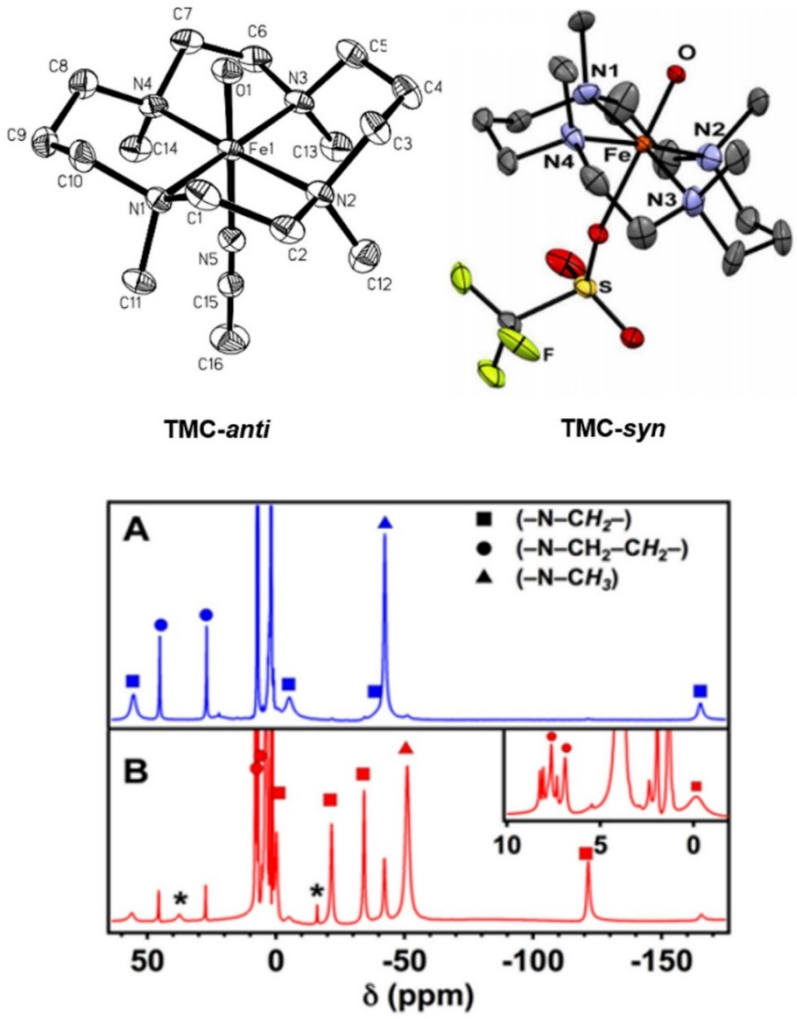

Fig. S2. Top: Reported crystal structures of TMC-*anti* (ref 3) and TMC-*syn* (ref 4) complexes. **Bottom:** Distinct ^{1}H-NMR spectra of TMC-*anti* (A) *and* TMC-*syn* (B) isomers in CD_3CN (ref 4).

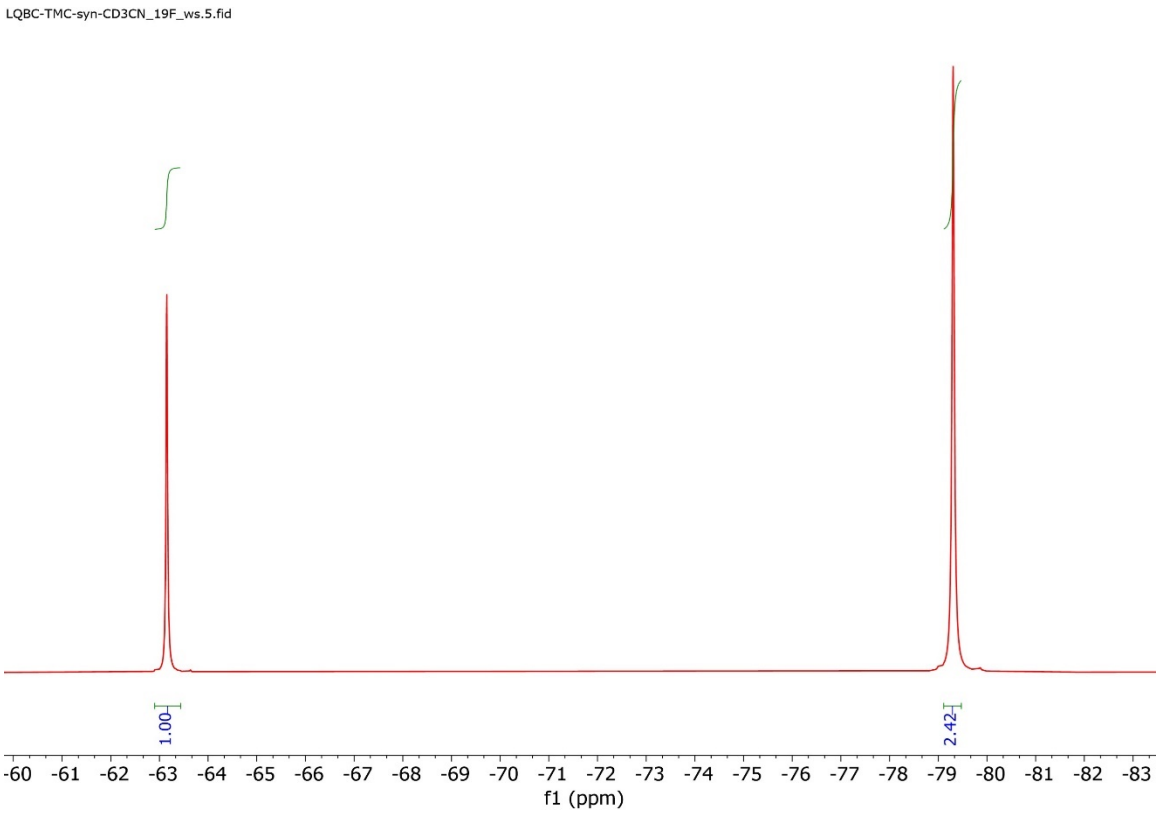

Fig. S3. ^{19}F-NMR spectrum of TMC-*syn* in CD_3CN at 25 °C with trifluorotoluene (δ = -63.7 ppm) as an internal standard. The peak at δ = -79 ppm for free triflates indicates that the bound triflate in the crystal structure is displaced by MeCN.

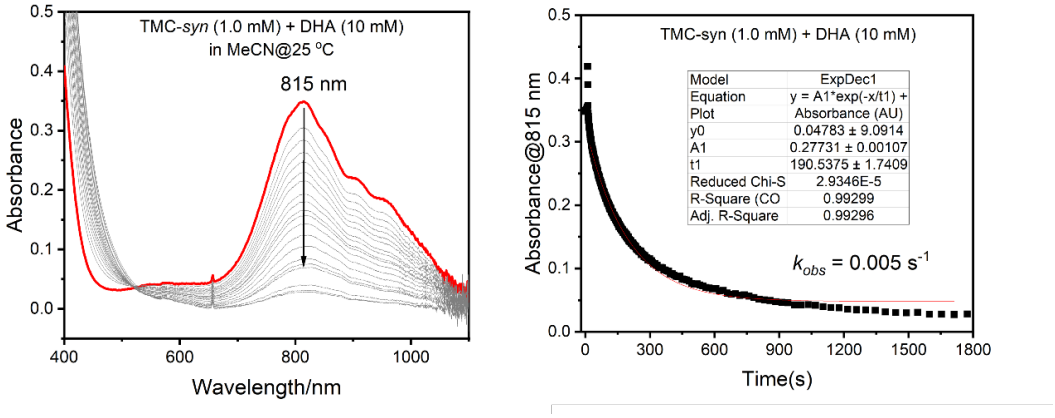

Fig. S4a. Spectral changes (left) and time trace monitored at 815 nm (right) during the HAT reaction of TMC-syn with DHA in MeCN at 25 °C.

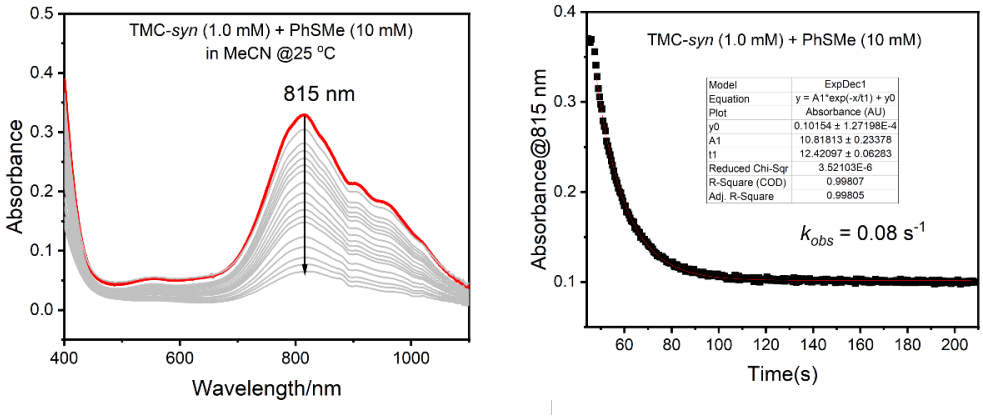

Fig. S4b. Spectral changes (left) and time trace monitored at 815 nm (right) during the OAT reaction of TMC-syn with thioanisole in MeCN at 25 °C.

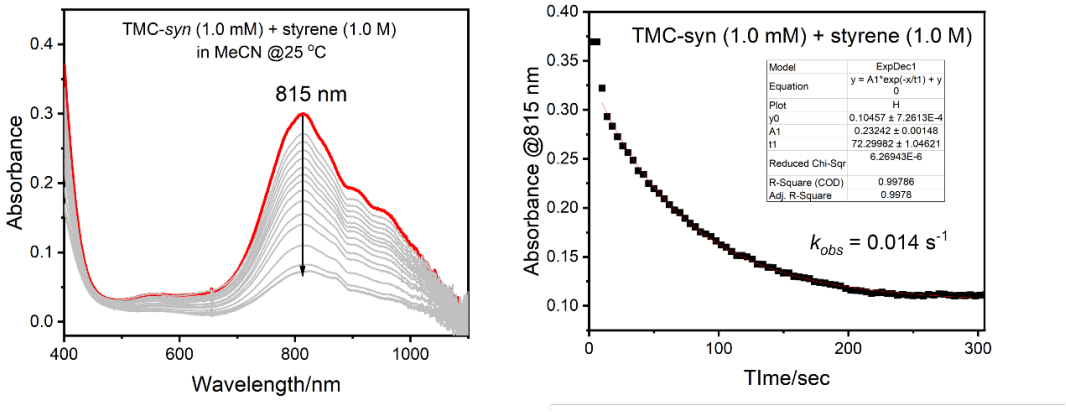

Fig. S4c. Spectral changes (left) and time trace monitored at 815 nm (right) during the OAT reaction of TMC-syn with styrene in MeCN at 25 °C.

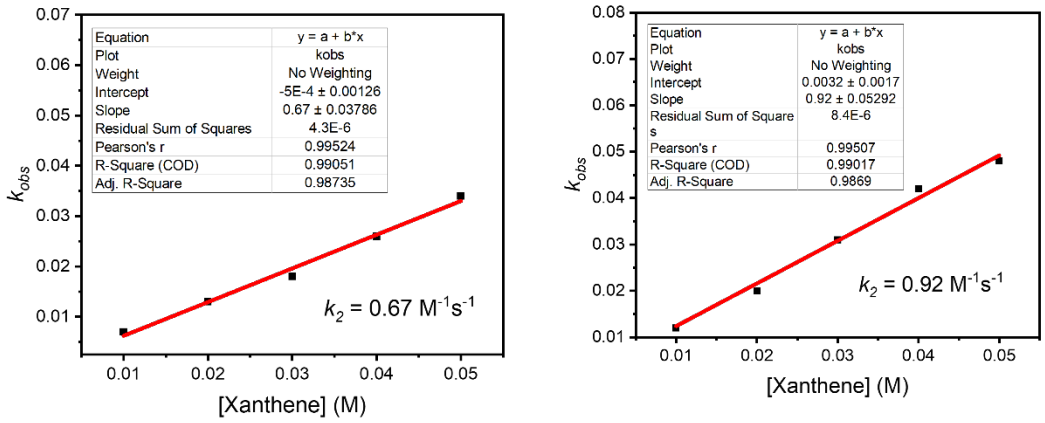

Fig. S5a. Plots of pseudo-first-order rate constants, k_{obs} (s^{-1}), against substrate concentrations to determine second-order rate constants, k_2 ($M^{-1}s^{-1}$), for the HAT reaction of TMC-*anti* (left) and TMC-*syn* (right) with xanthene in MeCN at 25 °C.

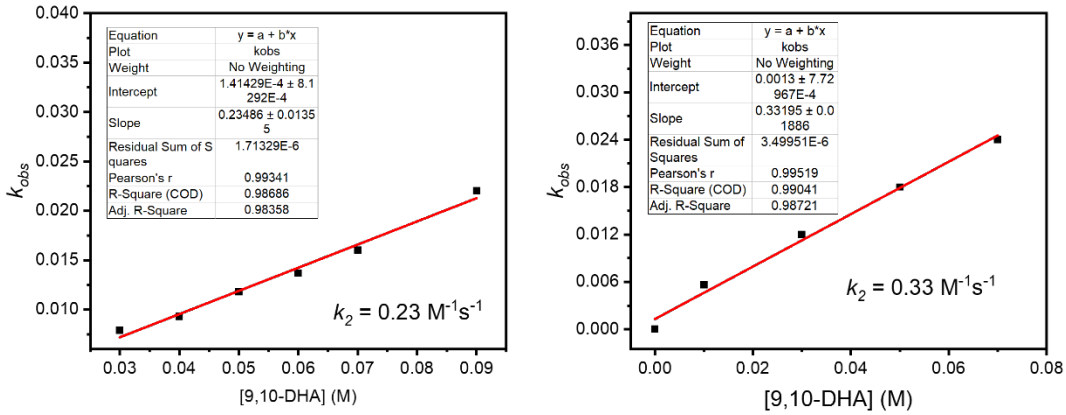

Fig. S5b. Plots of pseudo-first-order rate constants, k_{obs} (s^{-1}), against substrate concentrations to determine second-order rate constants, k_2 ($M^{-1}s^{-1}$), for the HAT reaction of TMC-*anti* (left) and TMC-*syn* (right) with 9,10-dihydroanthracene in MeCN at 25 °C.

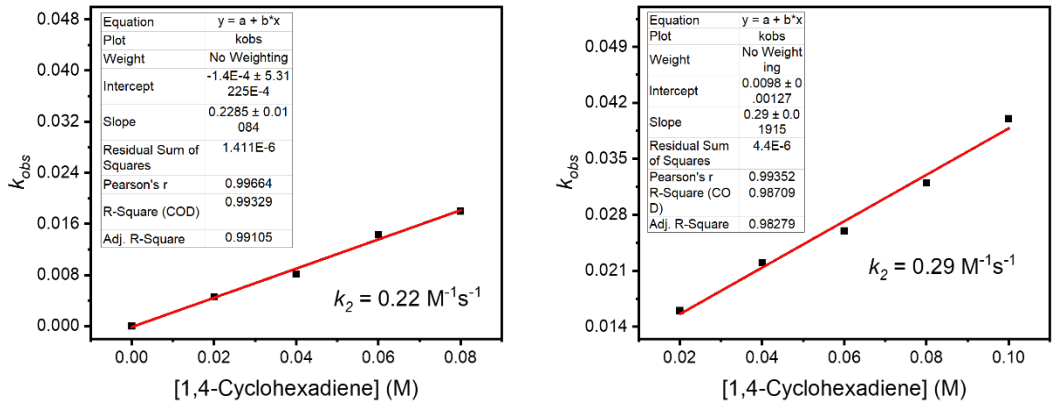

Fig. S5c. Plots of pseudo-first-order rate constants, k_{obs} (s^{-1}), against substrate concentrations to determine second-order rate constants, k_2 ($M^{-1}s^{-1}$), for the HAT reaction of TMC-*anti* (left) and TMC-*syn* (right) with 1,4-cyclohexadiene in MeCN at 25 °C.

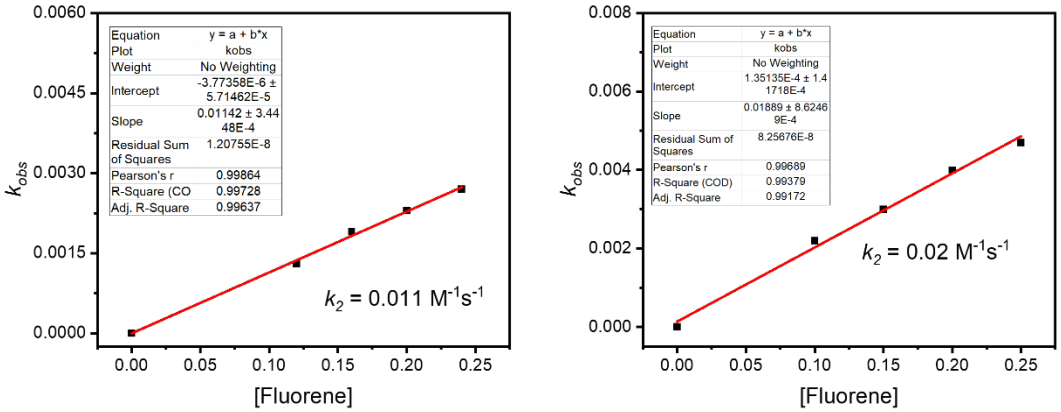

Fig. S5d. Plots of pseudo-first-order rate constants, k_{obs} (s^{-1}), against substrate concentrations to determine second-order rate constants, k_2 ($M^{-1}s^{-1}$), for the HAT reaction of TMC-*anti* (left) and TMC-*syn* (right) with fluorene in MeCN at 25 °C.

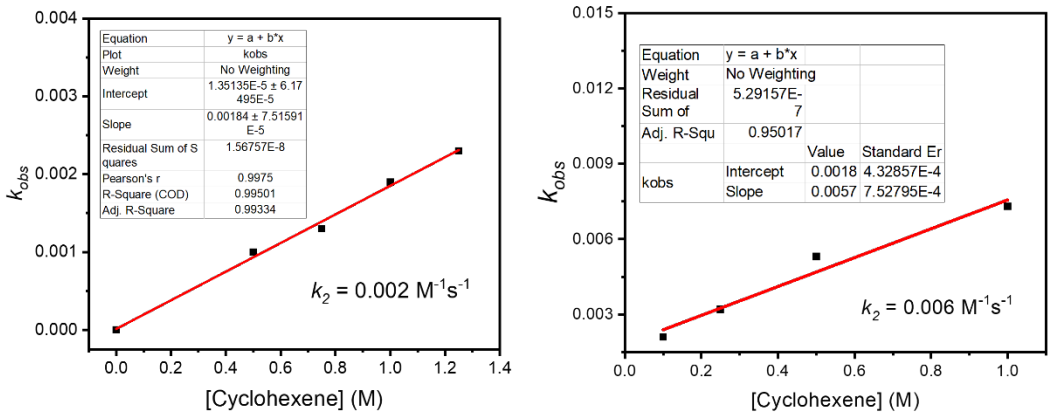

Fig. S5e. Plots of pseudo-first-order rate constants, k_{obs} (s^{-1}), against substrate concentrations to determine second-order rate constants, k_2 ($M^{-1}s^{-1}$), for the HAT reaction of TMC-*anti* (left) and TMC-*syn* (right) with cyclohexene in MeCN at 25 °C.

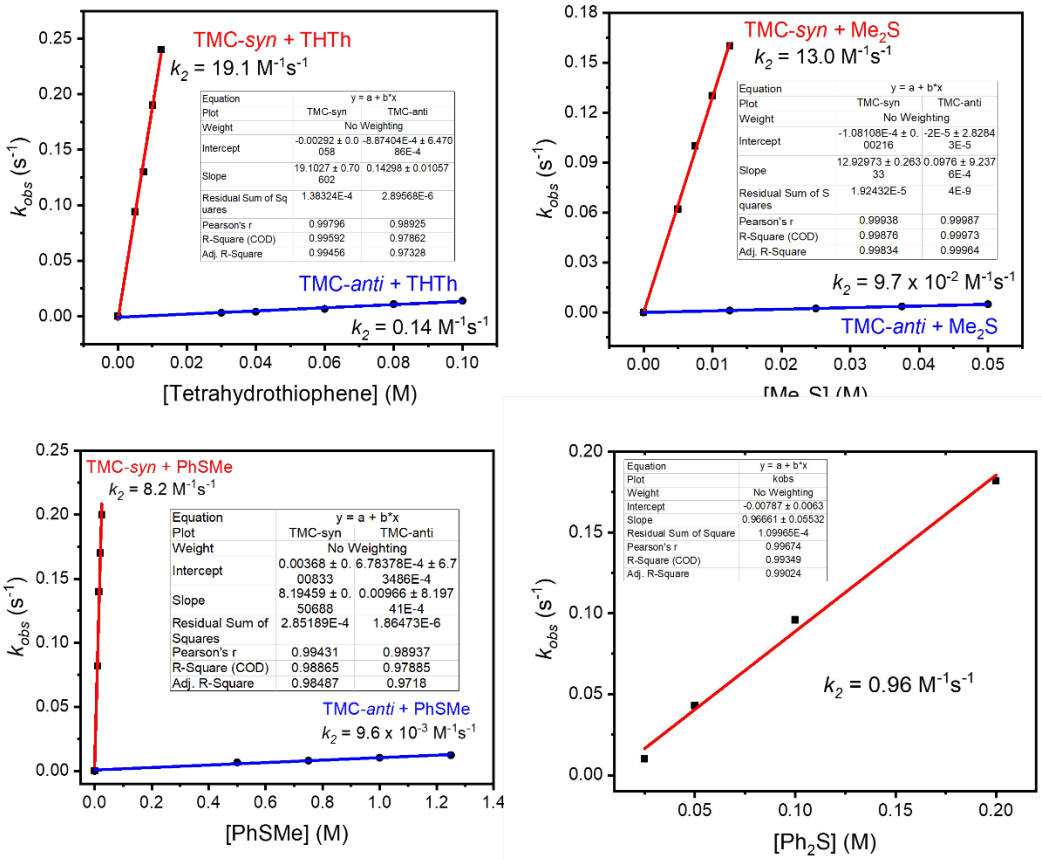

Fig. S6. Plots of pseudo-first order rate constant, k_{obs} (s^{-1}), against substrate concentrations to determine second-order rate constant, k_2 ($M^{-1}s^{-1}$), for the OAT reaction of TMC-*anti* (blue) and TMC-*syn* (red) with tetrahydrothiophene, dimethylsulfide (Me_2S), thioanisole (PhSMe), and diphenylsulfide (Ph_2S)

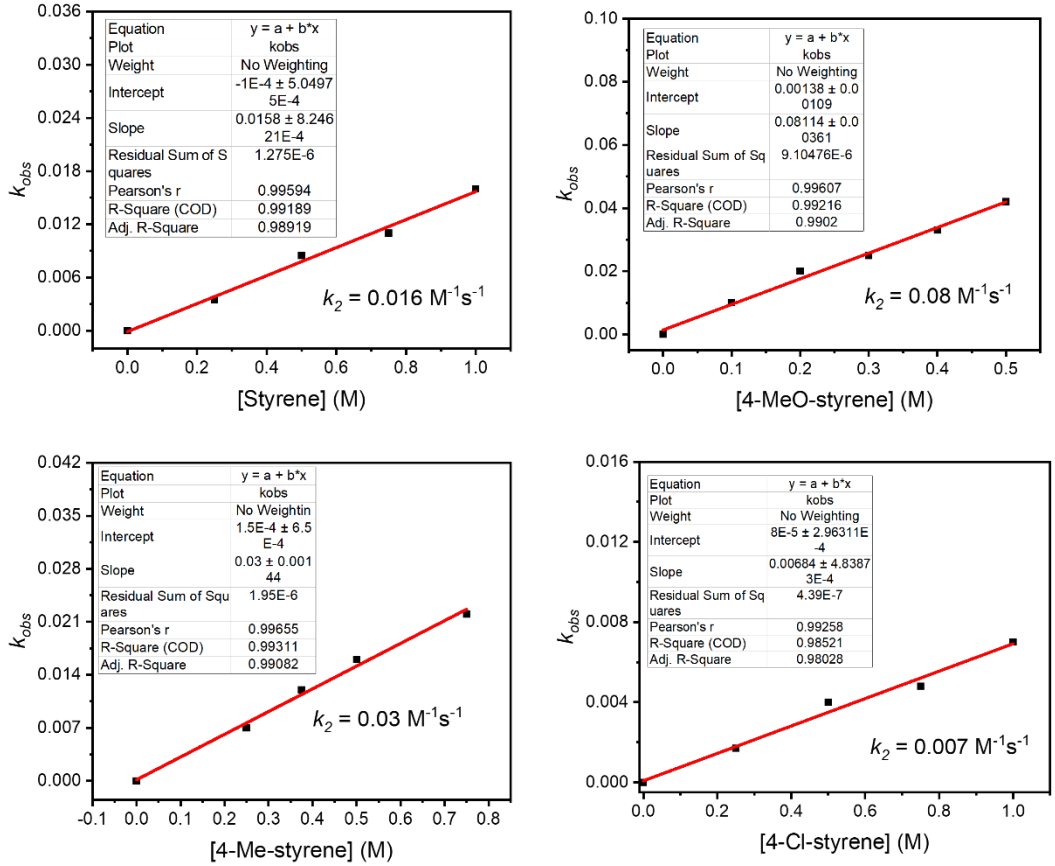

Fig. S7a. Plots of pseudo-first-order rate constants, k_{obs} (s^{-1}), against substrate concentrations to determine second-order rate constants, k_2 ($M^{-1}s^{-1}$), values for the OAT reactions of TMC-*syn* with 4-X-styrenes in MeCN at 25 °C.

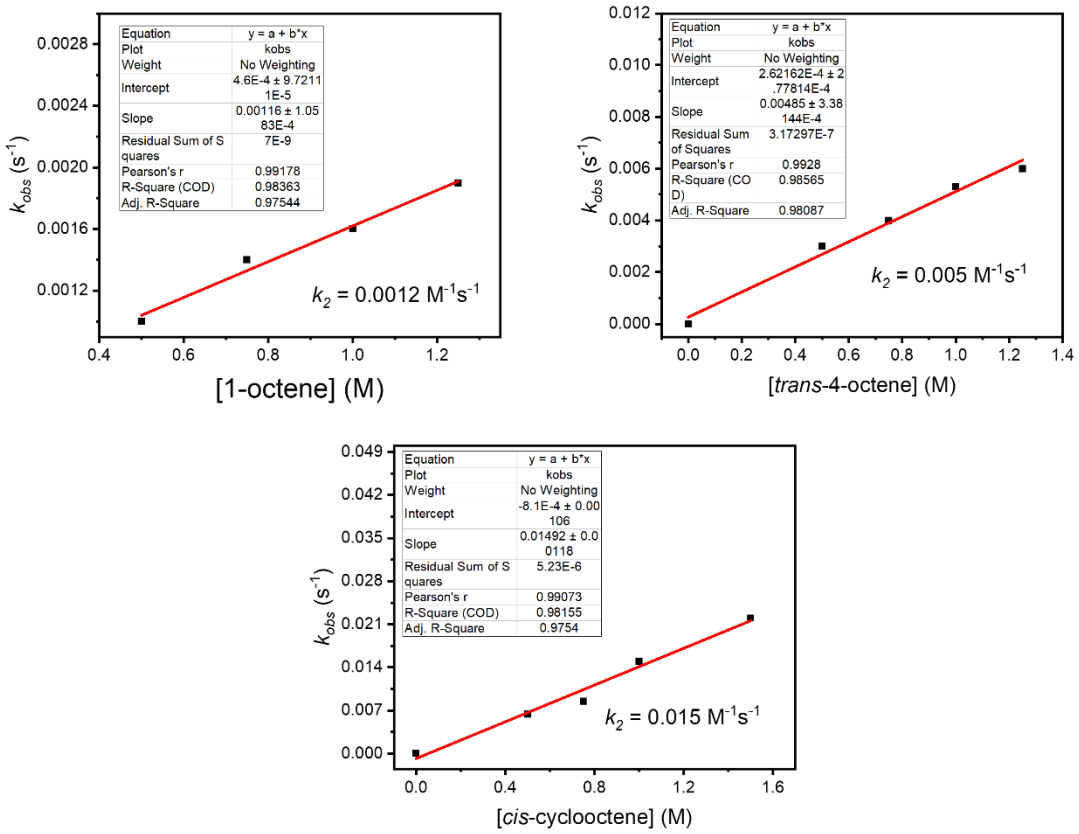

Fig. S7b. Plots of pseudo-first-order rate constants, k_{obs} (s^{-1}), against substrate concentrations to determine second-order rate constants, k_2 ($M^{-1}s^{-1}$), for the OAT reactions of TMC-*syn* with 1-octene, *trans*-4-octene, and *cis*-cyclooctene in MeCN at 25 °C.

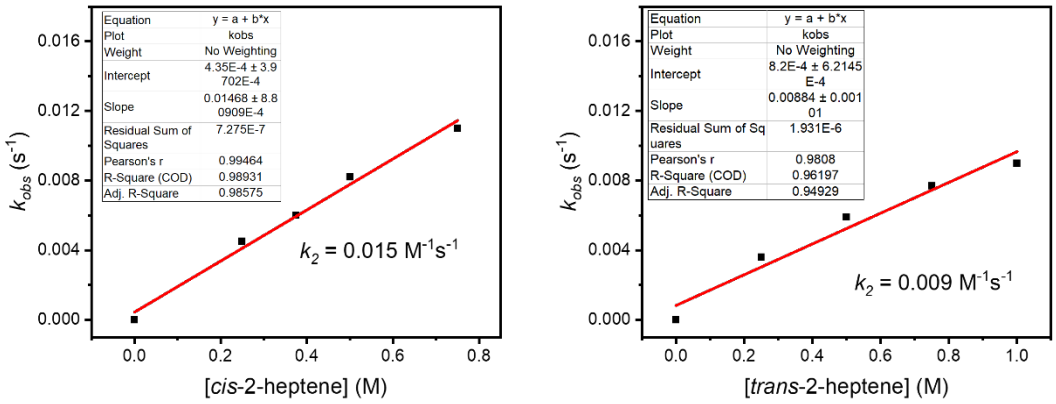

Fig. S7c. Plots of pseudo-first-order rate constants, k_{obs} (s^{-1}), against substrate concentrations to determine second-order rate constants, k_2 ($M^{-1}s^{-1}$), for the OAT reactions of TMC-*syn* with *cis*- and *trans*-2-heptene in MeCN at 25 °C.

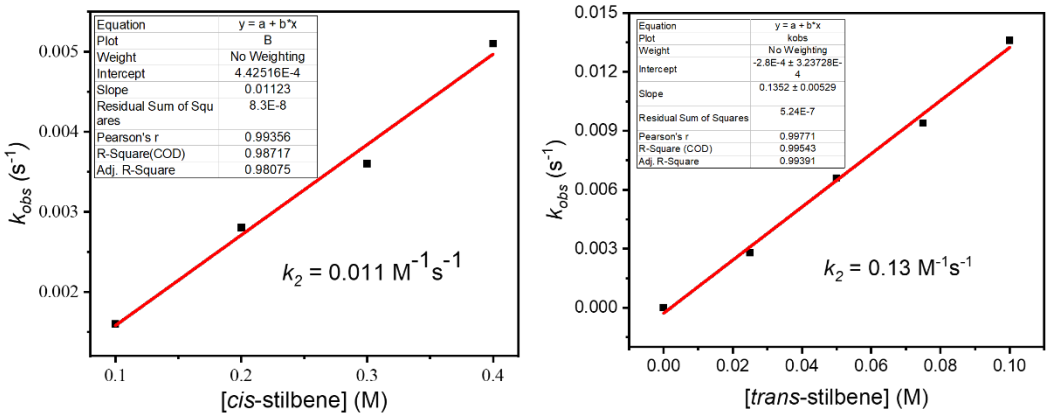

Fig. S7d. Plots of pseudo-first-order rate constants, k_{obs} (s^{-1}), against substrate concentrations to determine second-order rate constants, k_2 ($M^{-1}s^{-1}$), for the OAT reactions of TMC-*syn* with *cis*-stilbene (left) and *trans*-stilbene (right) in MeCN at 25 °C.

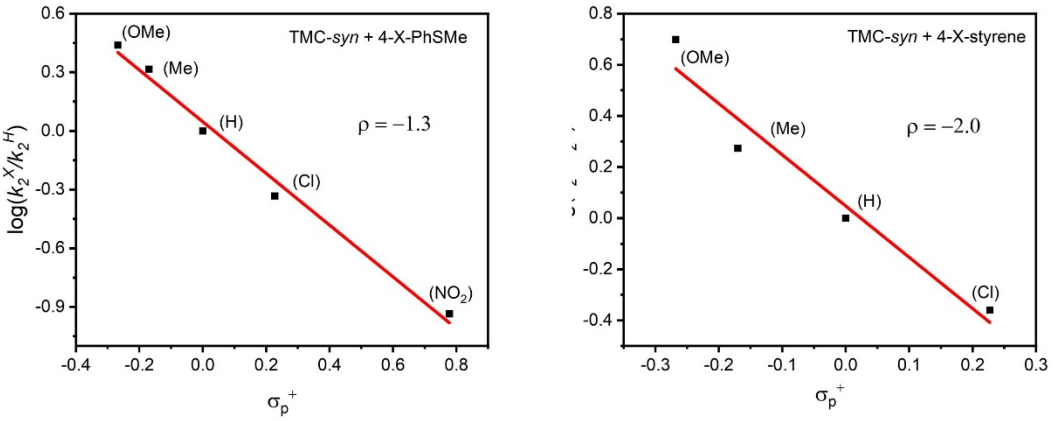

Fig. S8. Plots of $\log(k_2^X/k_2^H)$ values vs σ_ρ^+ values for para-substituted thioanisoles (4-X-ArSMe; where X = H, -Me, -OMe, -Cl and -NO_2) and para-substituted styrenes (4-X-styrenes; where X = H, -Me, -OMe, and -Cl) to obtain Hammett ρ values.

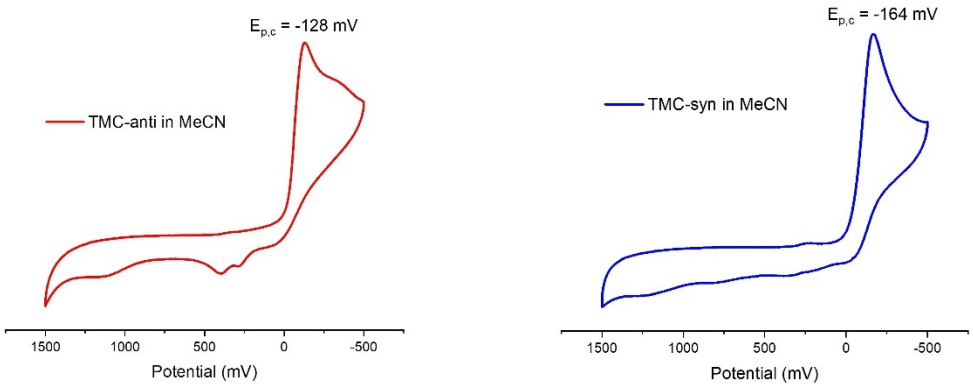

Fig. S9. Cyclic voltammograms of TMC-*anti* and TMC-*syn* in CH_3CN at 25 °C using GC as working electrode, Pt wire as counter electrode, and Ag wire in 0.1 M Bu_4NPF_6 solution as reference electrode. The difference in cathodic peak current is only 36 mV.

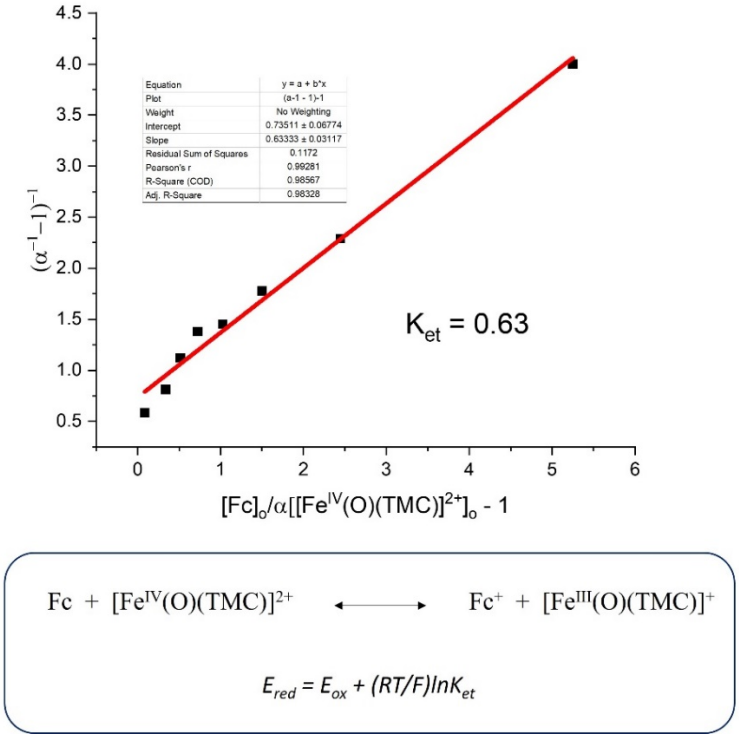

Fig. S10. Spectral redox titration of TMC-*syn* using ferrocene. The E_{red} value for TMC-*syn* is found to be E_{red} = 0.36 V vs. SCE at 25 °C. (following Fukuzumi's method, ref 28).

GC-MS spectra of the product formation in the HAT reactions of TMC-*syn*

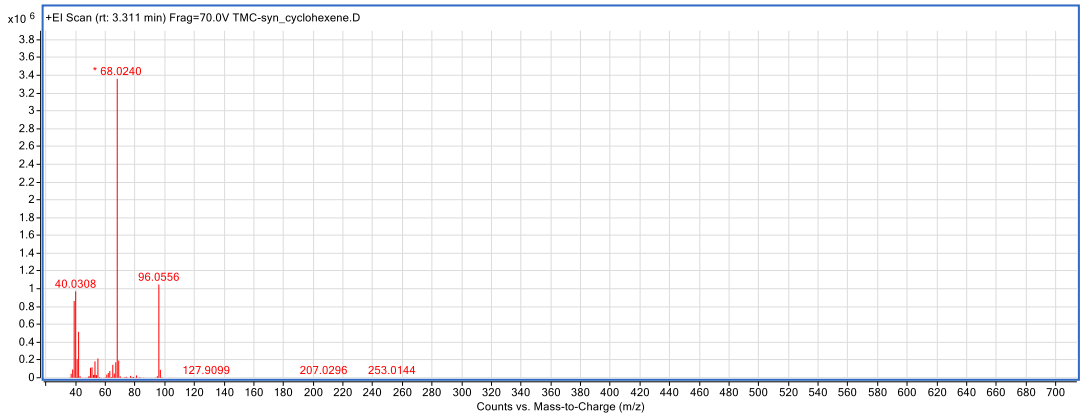

Fig. S11a. 2-cyclohexenol as the major product formed in the HAT reaction of TMC-*syn* with cyclohexene in CH_3CN at 25 °C.

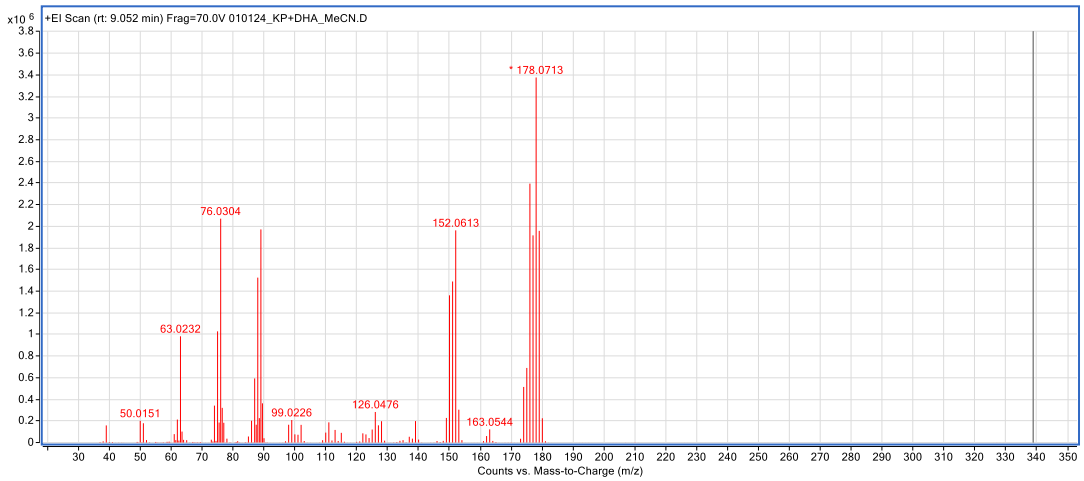

Fig. S11b. Anthracene as the major product formed in the HAT reaction of TMC-*syn* with 9,10-dihydroanthracene in CH_3CN at 25 °C.

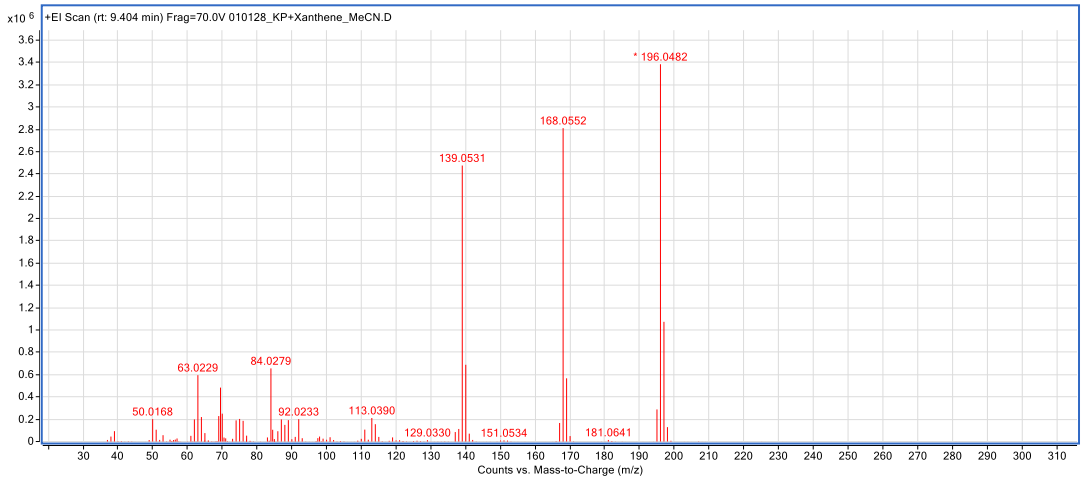

Fig. S11c. Xanthone as the only product formed in the HAT reaction of TMC-*syn* with xanthene in CH_3CN at 25 °C.

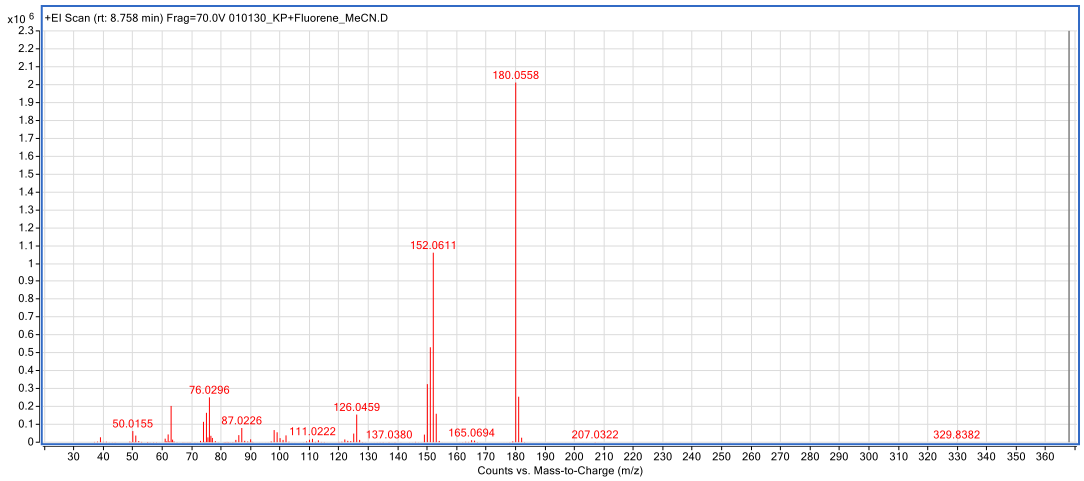

Fig. S11d. Fluorenone as the only product formed in the HAT reaction of TMC-*syn* with fluorene in CH_3CN at 25 °C.

GC-MS spectra of product formation in OAT reactions of TMC-*syn* with sulfides

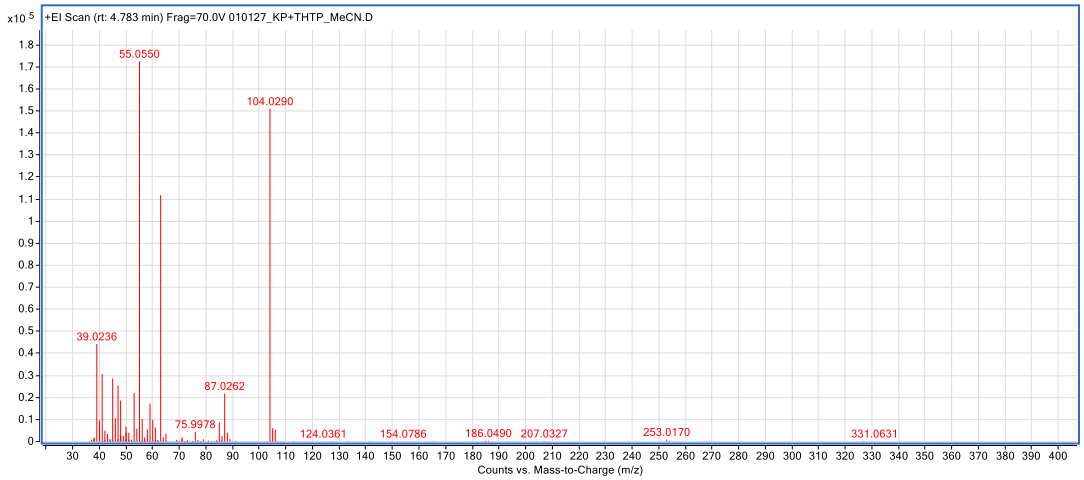

Fig. S12a. Tetrahydrothiophene oxide as the only product formed in the OAT reaction of TMC-*syn* with tetrahydrothiophene in CH_3CN at 25 ºC.

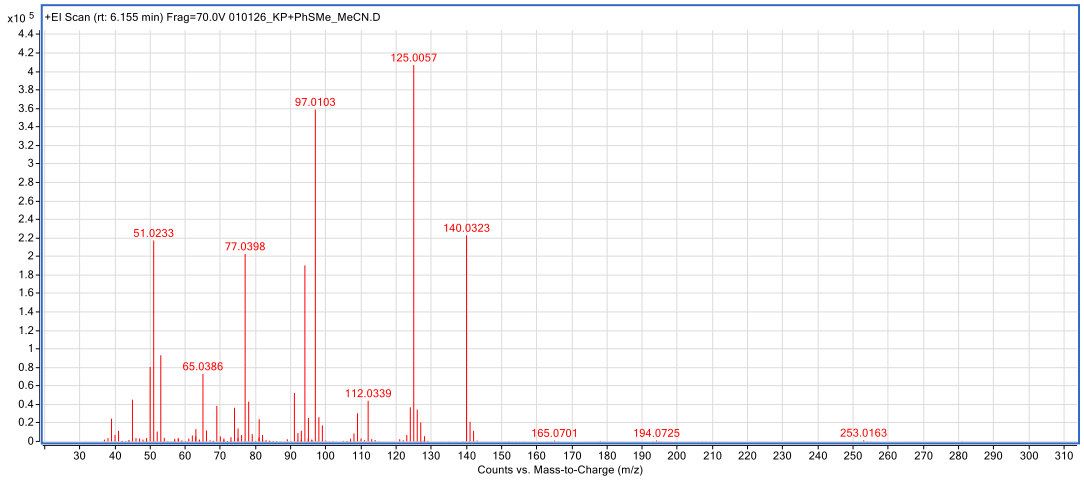

Fig. S12b. Methyl phenyl sulfoxide as the only product formed in the OAT reaction of TMC-*syn* with thioanisole in CH_3CN at 25 ºC.

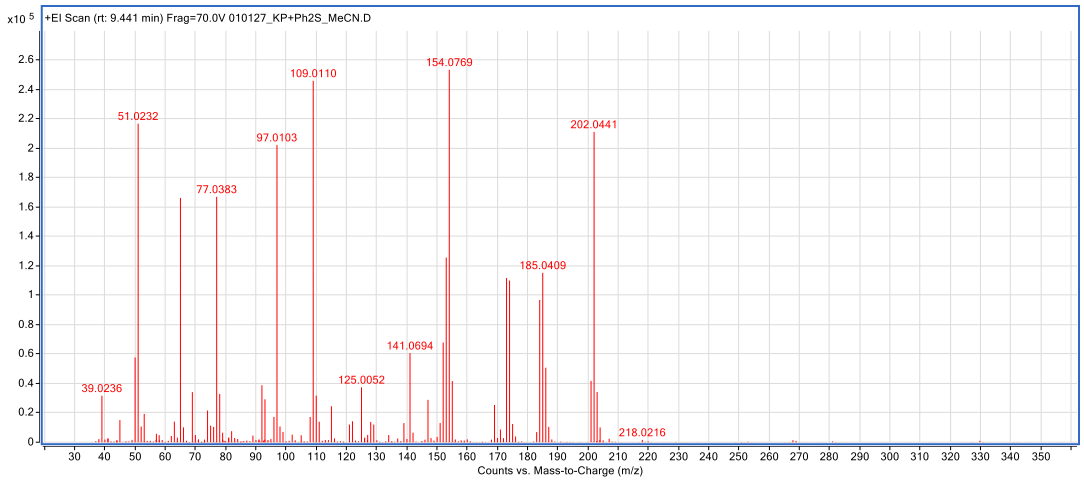

Fig. S12c. Diphenyl sulfoxide as the only product formed in the OAT reaction of TMC-*syn* with diphenyl sulfide in CH_3CN at 25 °C.

GC-MS spectra of product formation in OAT reactions of TMC-*syn* with olefines

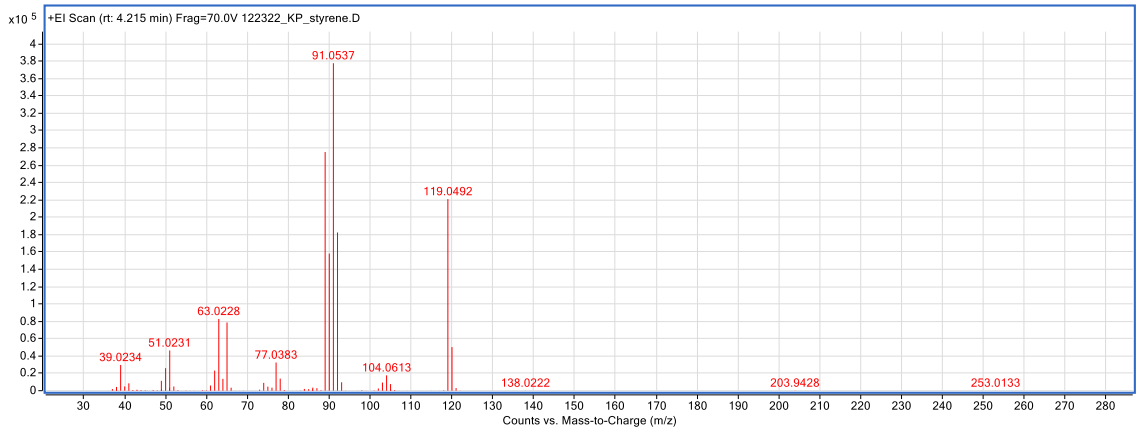

Fig. S13a. Styrene oxide product formation in the OAT reaction of TMC-*syn* with styrene in CH_3CN at 25 ºC.

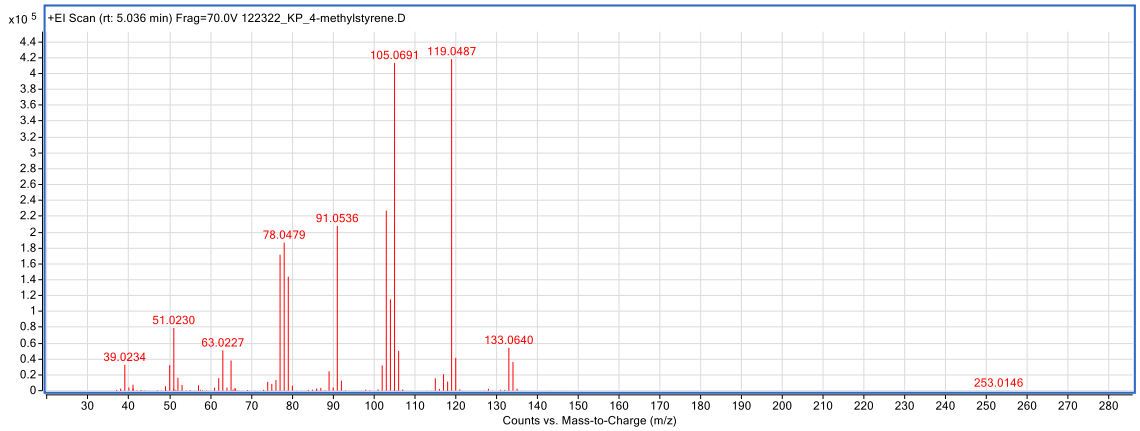

Fig. S13b. 4-methylstyrene oxide product formation in the OAT reaction of TMC-*syn* 4-methylstyrene in CH_3CN at 25 ºC.

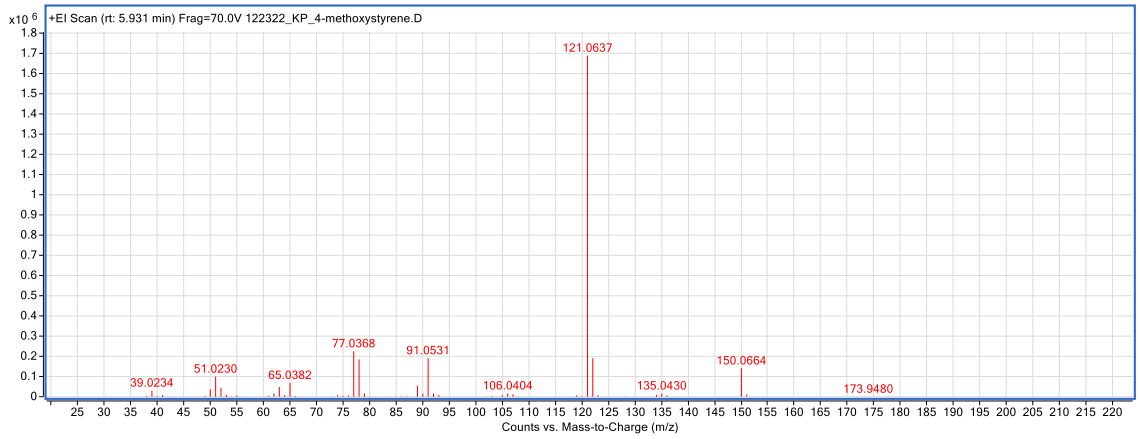

Fig. S13c. 4-methoxystyrene oxide product formation in the OAT reaction of TMC-*syn* 4-methoxystyrene in CH_3CN at 25 ºC.

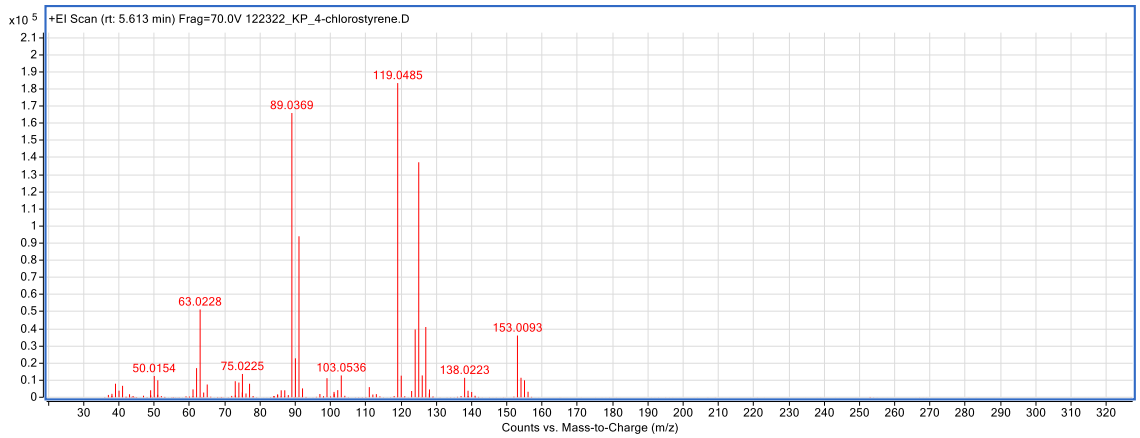

Fig. S13d. 4-chlorostyrene oxide product formation in the OAT reaction of TMC-*syn* with 4-chlorostyrene in CH_3CN at 25 °C.

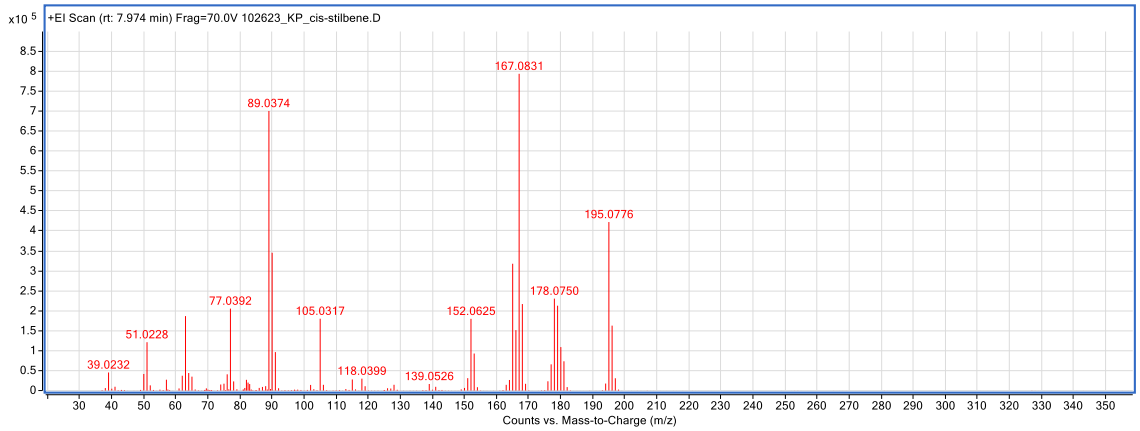

Fig. S13e. *cis*-stilbene epoxide product formation in the OAT reaction of TMC-*syn* with *cis*-stilbene in CH_3CN at 25 °C.

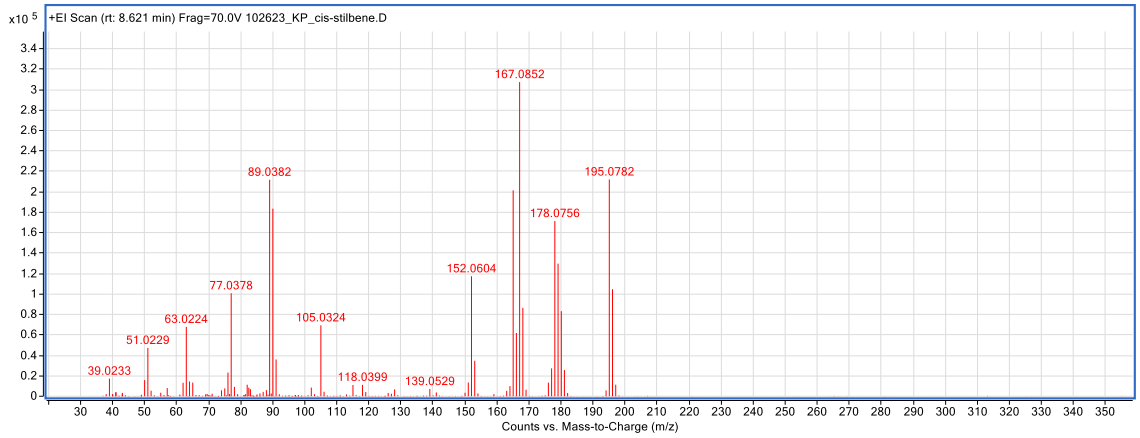

Fig. S13f. *trans*-stilbene epoxide product formation in the OAT reaction of TMC-*syn* with *cis*-stilbene in CH_3CN at 25 °C.

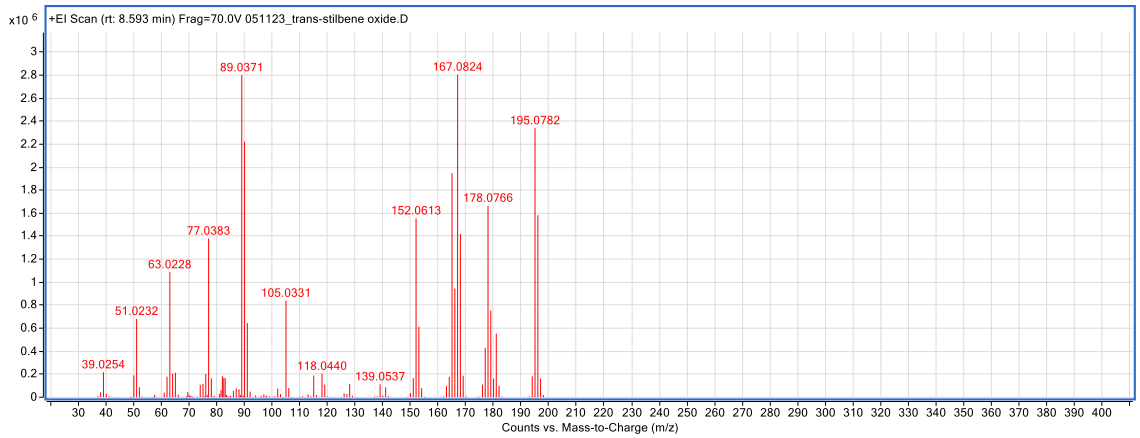

Fig. S13g. *trans*-stilbene epoxide product formation in the OAT reaction of TMC-*syn* with *trans*-stilbene in CH_3CN at 25 °C.

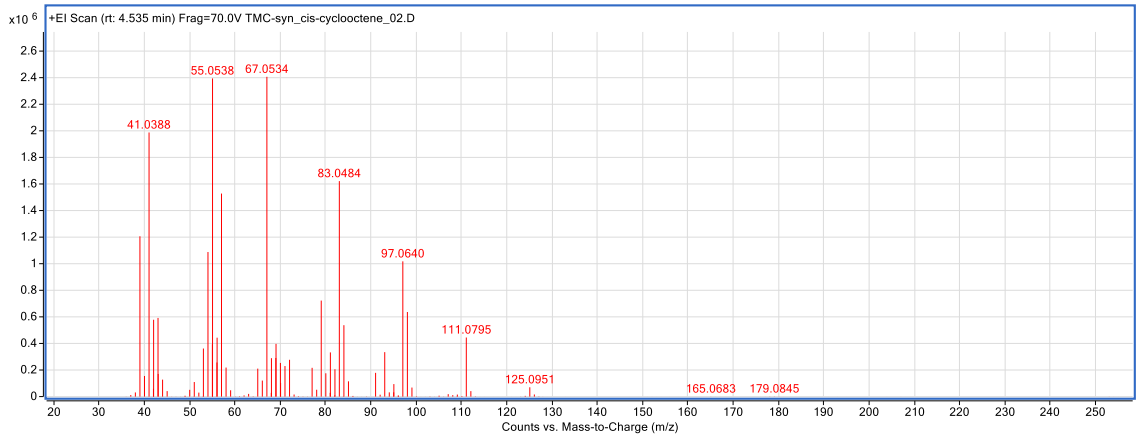

Fig. S13h. *cis*-cyclooctene epoxide product formation in the OAT reaction of TMC-*syn* with *cis*-cyclooctene in CH_3CN at 25 °C.

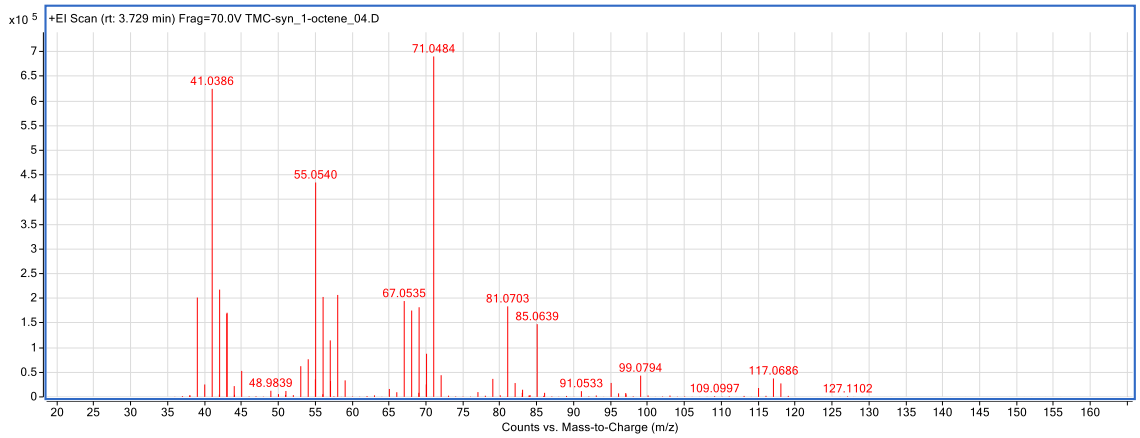

Fig. S13i. 1-octene epoxide product formation in the OAT reaction of TMC-*syn* with 1-octene in CH_3CN at 25 °C.

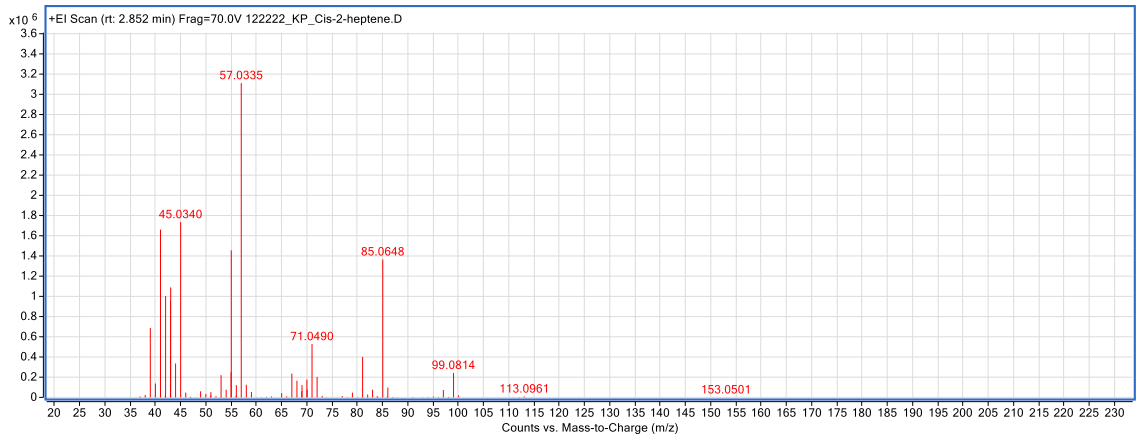

Fig. S13j. *cis*-2-heptene epoxide product formation in the OAT reaction of TMC-*syn* with *cis*-2-heptene in CH_3CN at 25 °C.

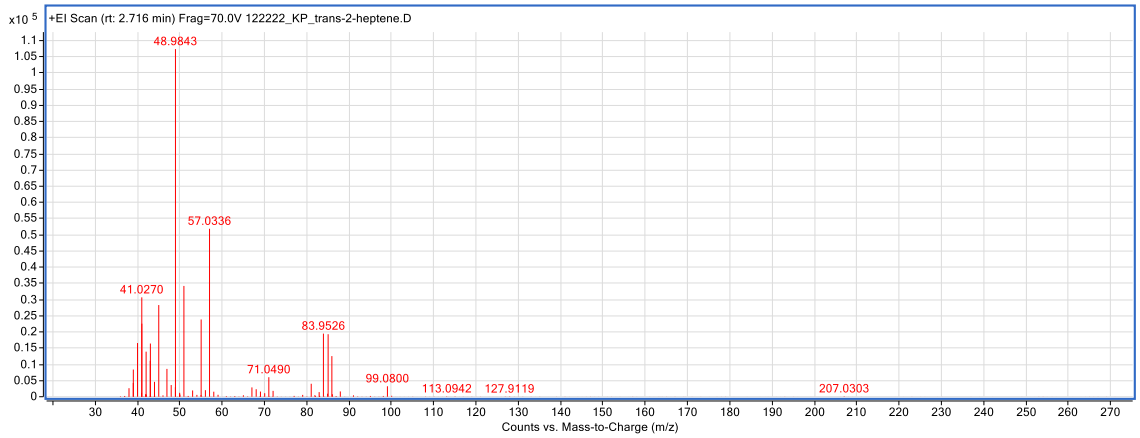

Fig. S13k. *trans*-2-heptene epoxide product formation in the OAT reaction of TMC-*syn* with *trans*-2-heptene in CH_3CN at 25 °C.

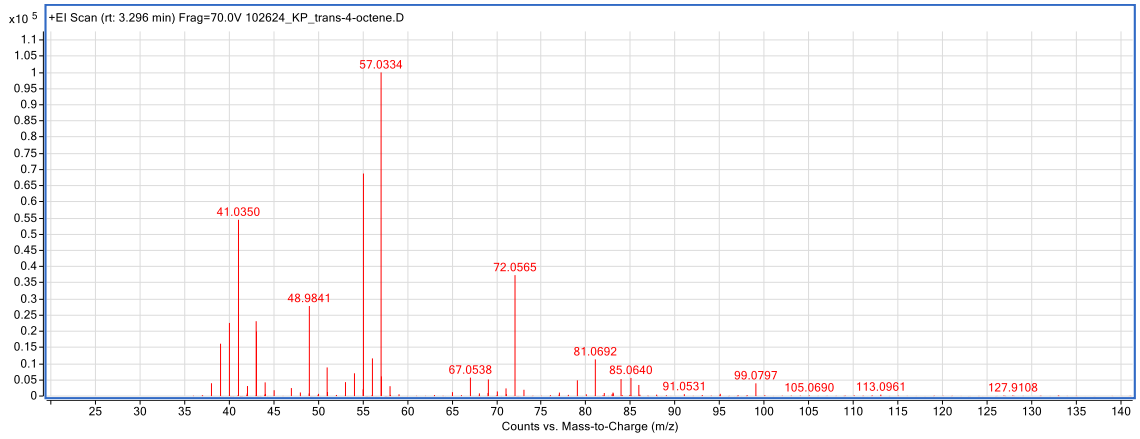

Fig. S13l. *trans*-4-octene oxide product formation in the OAT reaction of TMC-*syn* with *trans*-4-octene in CH_3CN at 25 °C.

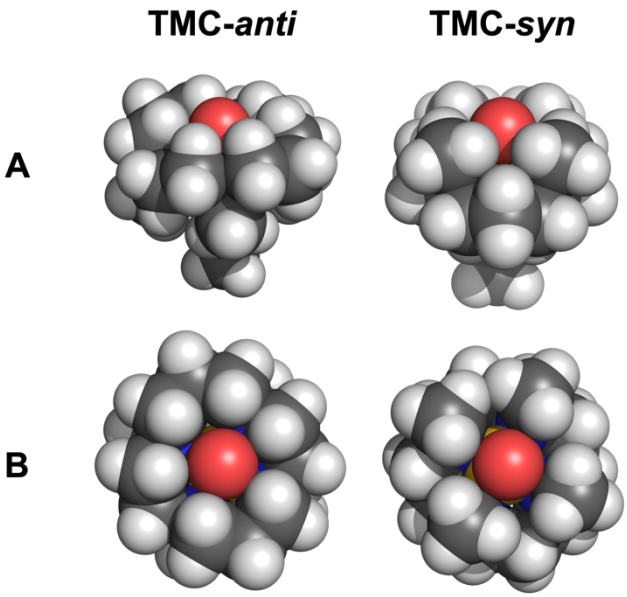

Fig. S14. van der Waals radii space-filling models for the two isomers showing the greater substrate accessibility of the oxo atom in the *syn* isomer. (A) side view; (B) top view.

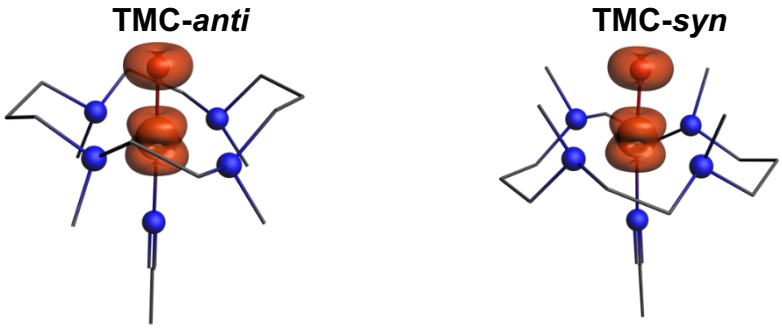

Fig. S15. DFT-derived spin densities of TMC-*anti* (left) and TMC-*syn* (right) complexes (isosurface = 0.02 e au^{-3})

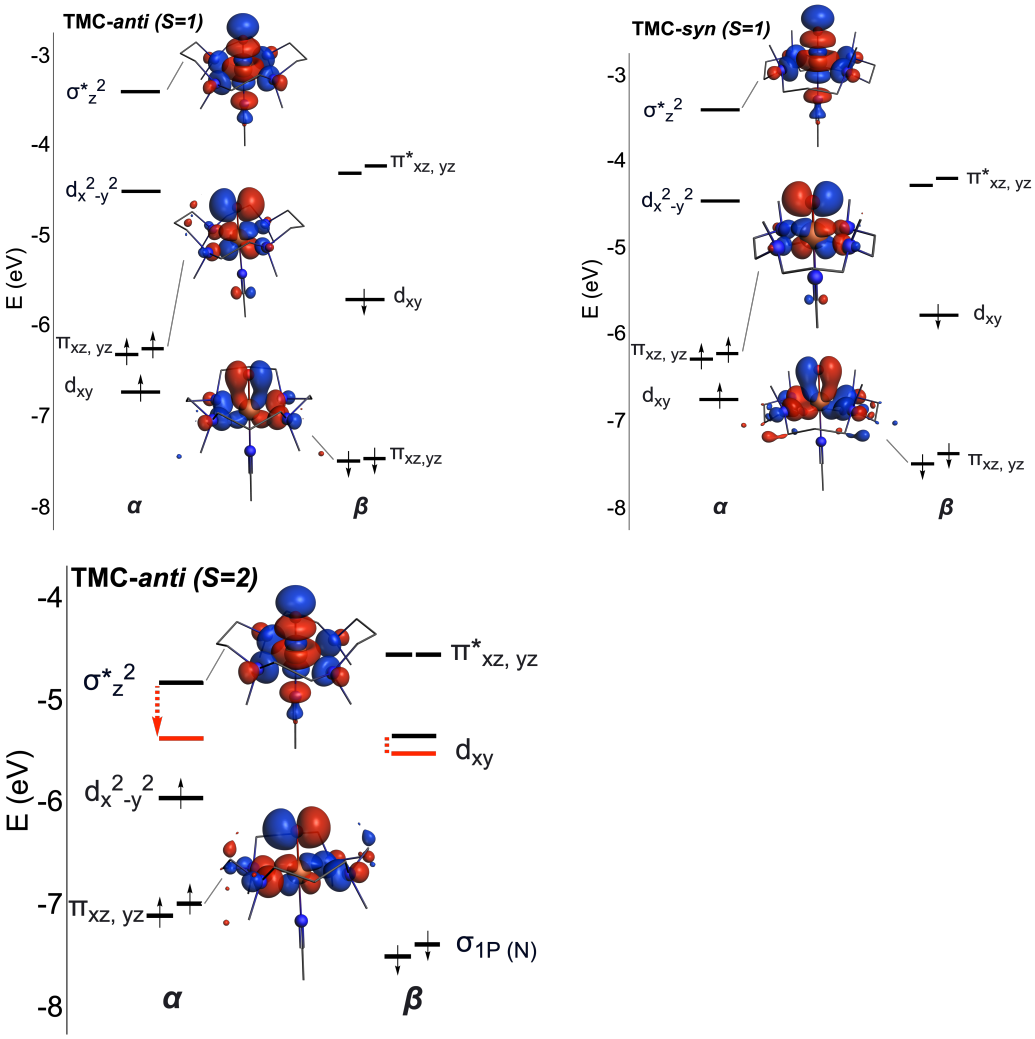

Fig. S16. Energies of MOs for *S* = 1 (top), for TMC-*anti* (left), TMC-*syn* (right). Energies of frontier MOs for the *S* = 2 (bottom) for TMC-*anti*. Indicated in red is the lowering of s* and d_{xy} orbitals due to the lengthening of Fe-$NCCH_3$ bond to 2.5 Å. (MO density isosurface values (± 0.035 e au^{-3}). In each panel, *α* and *β* spin orbitals are shown on the left and right, respectively.

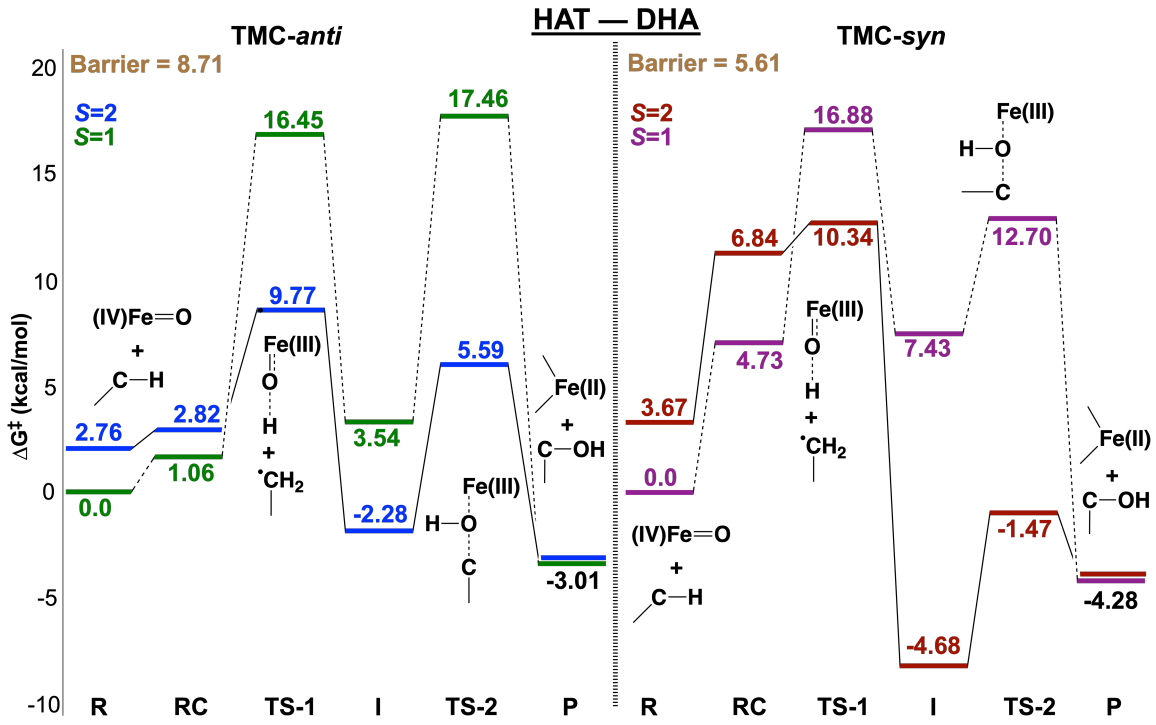

Fig. S17a. Potential Energy Surface for HAT to DHA, where R is the energy of reactants (TMC-*syn/anti* + DHA substrate), RC = reactant complex, TS-1 = first transition state, I = intermediate, TS-2 = second transition state and P is the energy of products. The transition energy barrier at the top left of each panel represents the $\Delta G^{\ddagger}$ = (TS, *S* = 2) - (RC, *S* = 1).

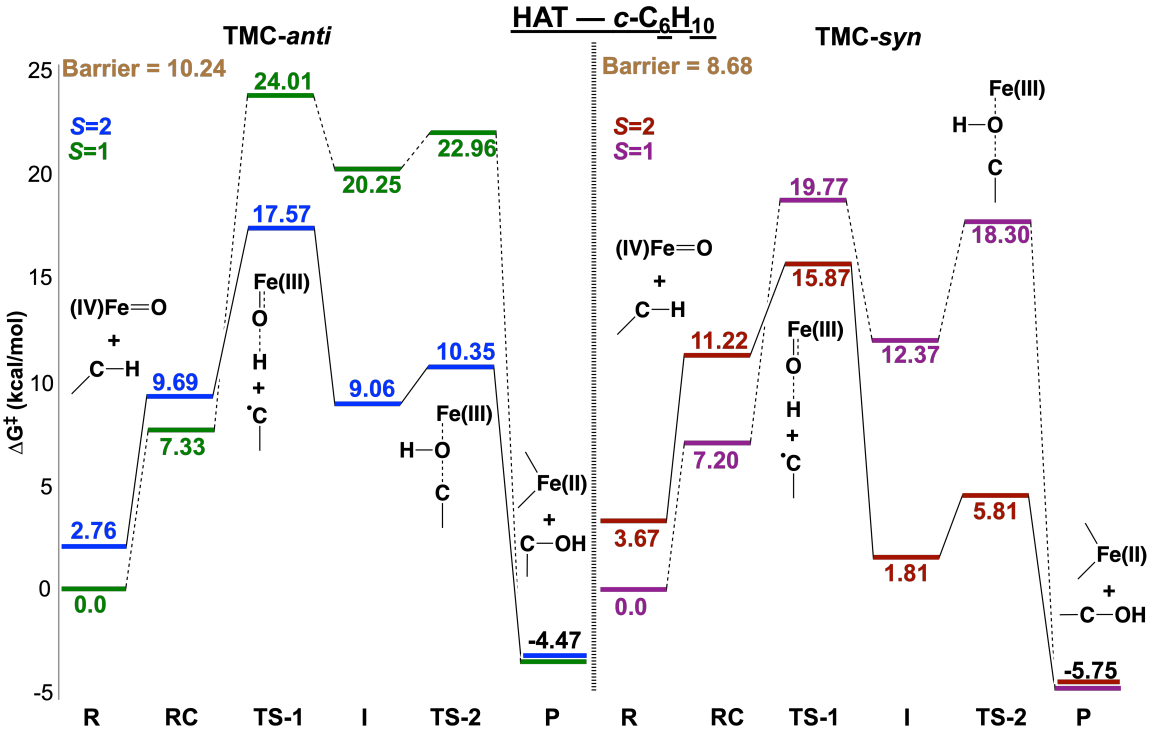

Fig. S17b. Potential Energy Surface for HAT to cyclohexene where R is the energy of reactants (TMC-*syn/anti* + *c*-C_6H_{10} substrate), RC = reactant complex, TS-1 = first transition state, I = intermediate, TS-2 = second transition state and P is the energy of products. The transition energy barrier at the top left of each panel represents the $\Delta G^{\ddagger}$ = (TS, *S* = 2) - (RC, *S* = 1).

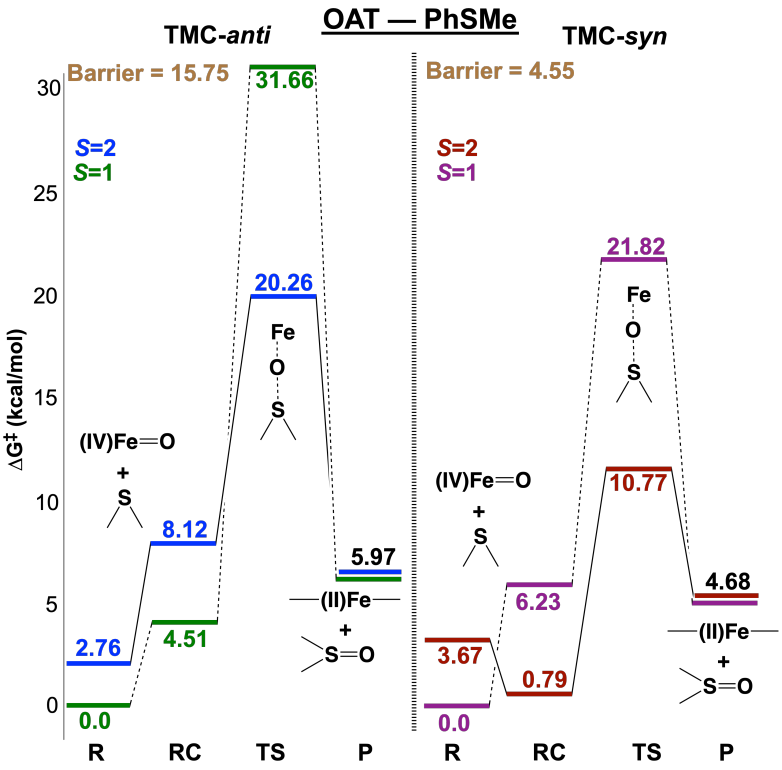

Fig. S18. Potential Energy Surface for OAT to thioanisole. Where R is the energy of reactants (TMC-*syn/anti* + PhSMe), RC = reactant complex, TS-1 = first transition state, and P is the energy of products. The transition energy barrier at the top left of each panel represents the $\Delta G^{\ddagger}$ = (TS, *S* = 2) - (RC, *S* = 1).

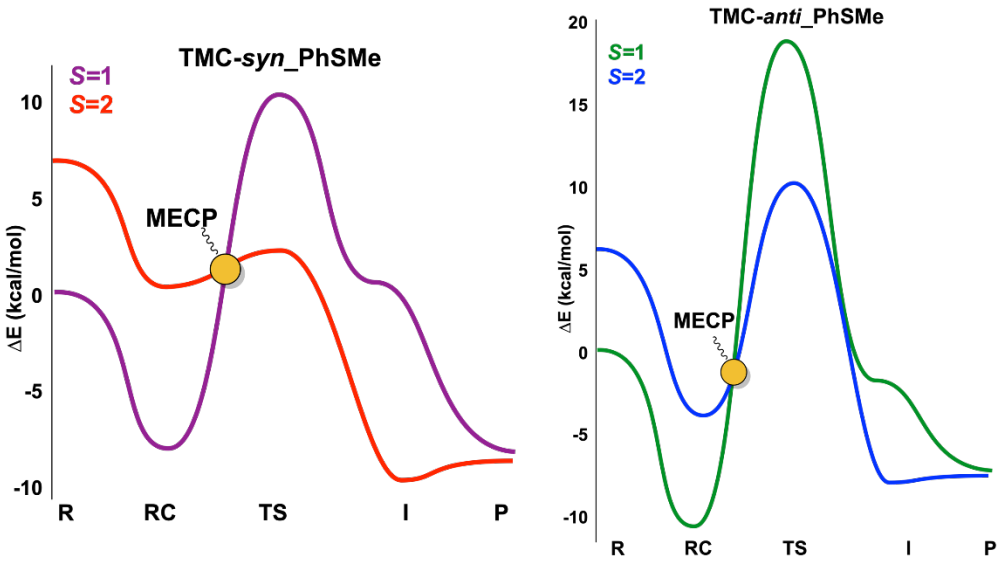

Fig. S19. Electronic energy surface (kcal·mol^{-1}, B97-D3/TZ2P + COSMO/ZORA) for *S* = 1 and *S* = 2 states for the OAT reaction of TMC-*syn* (left) and TMC-*anti* (right) with thioanisole. Indicated with the yellow sphere is the minimum energy crossing point (MECP), where the two spin-state surfaces cross.

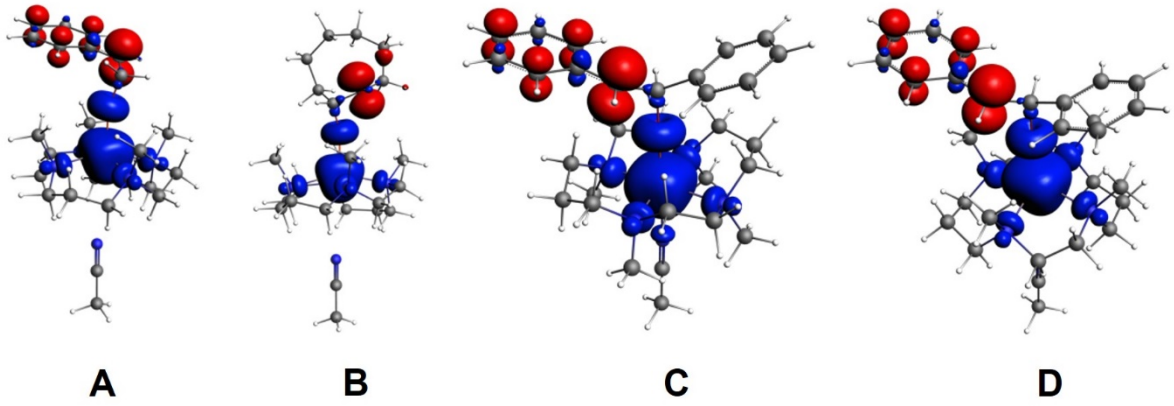

Fig. S20. Spin density plots (isosurface 0.005 e au^{-3})

A = KP-styrene intermediate (*S* = 2)

B = KP-cyclooctene intermediate (*S* = 2)

C = TP-*trans*-stilbene intermediate (*S* = 2)

D = KP-*trans*-stilbene intermediate (*S* = 2)

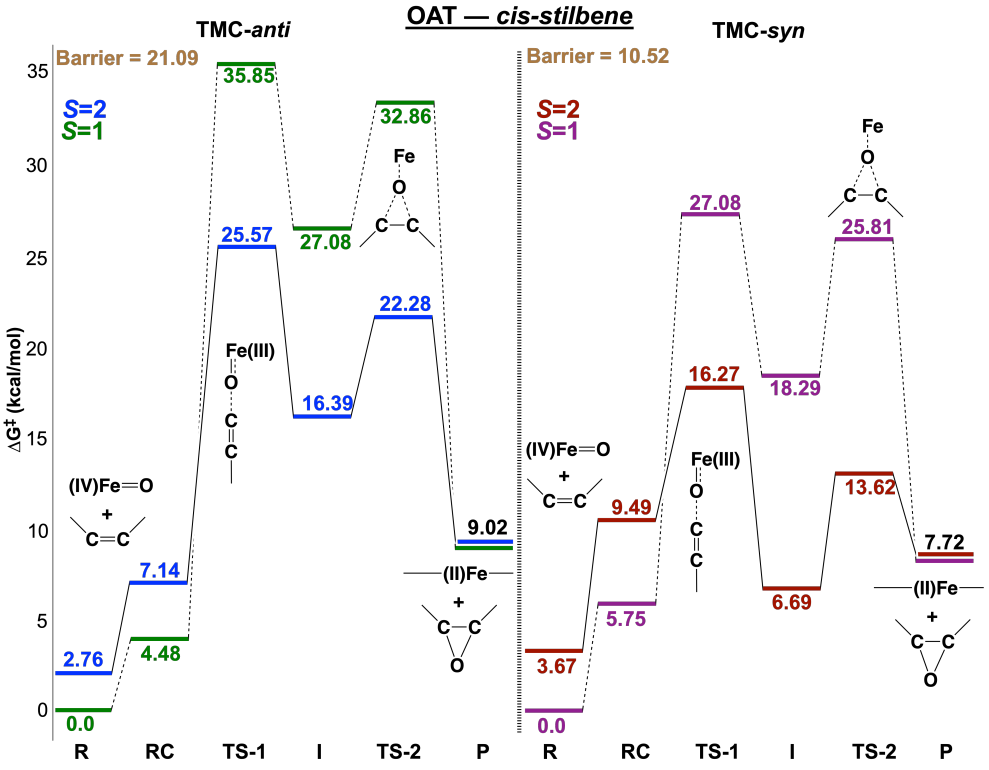

Fig. S21a. Potential Energy Surface for OAT to *cis*-stilbene, Where R is the energy of reactants (TMC-*syn/anti* + *cis*-stilbene), RC = reactant complex, TS-1 = first transition state, I = intermediate, TS-2 = second transition state and P is the energy of products. The transition energy barrier at the top left of each panel represents the $\Delta G^{\ddagger}$ = (TS, *S* = 2) - (RC, *S* = 1).

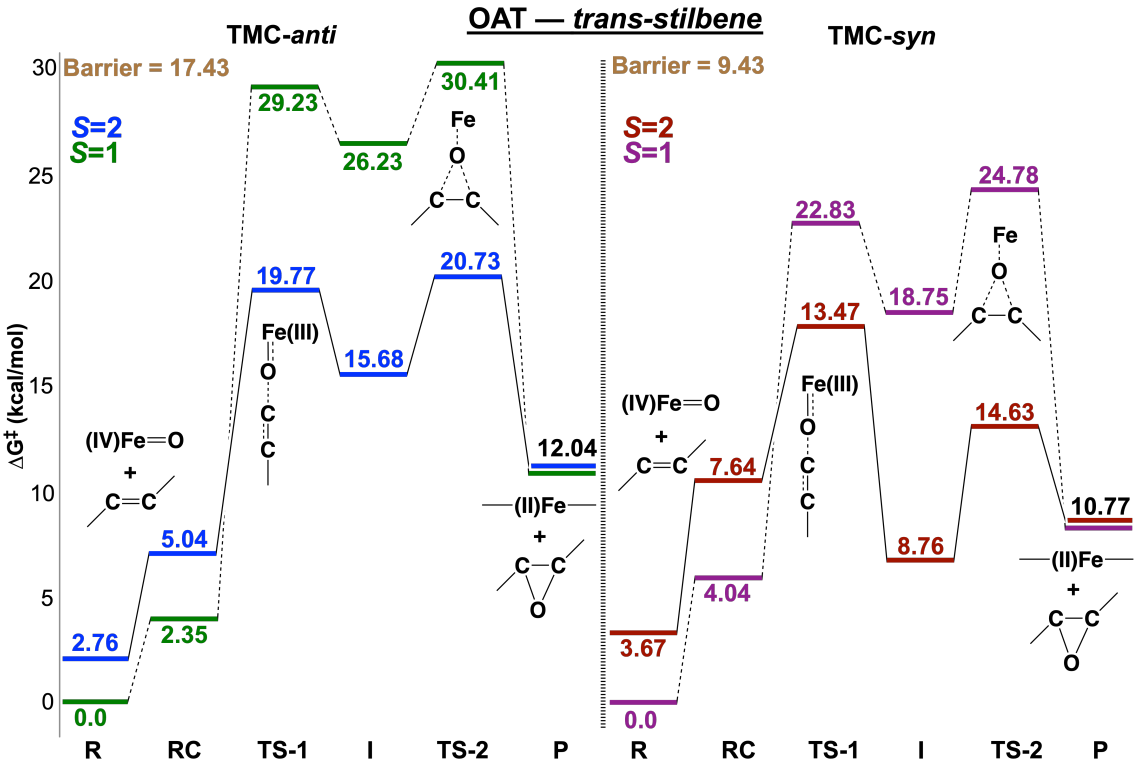

Fig. S21b. Potential Energy Surface for OAT to *trans*-stilbene. Where R is the energy of reactants (TMC-*syn/anti* + *trans*-stilbene), RC = reactant complex, TS-1 = first transition state, I = intermediate, TS-2 = second transition state and P is the energy of products. The transition energy barrier at the top left of each panel represents the $\Delta G^{\ddagger}$ = (TS, *S* = 2) - (RC, *S* = 1).

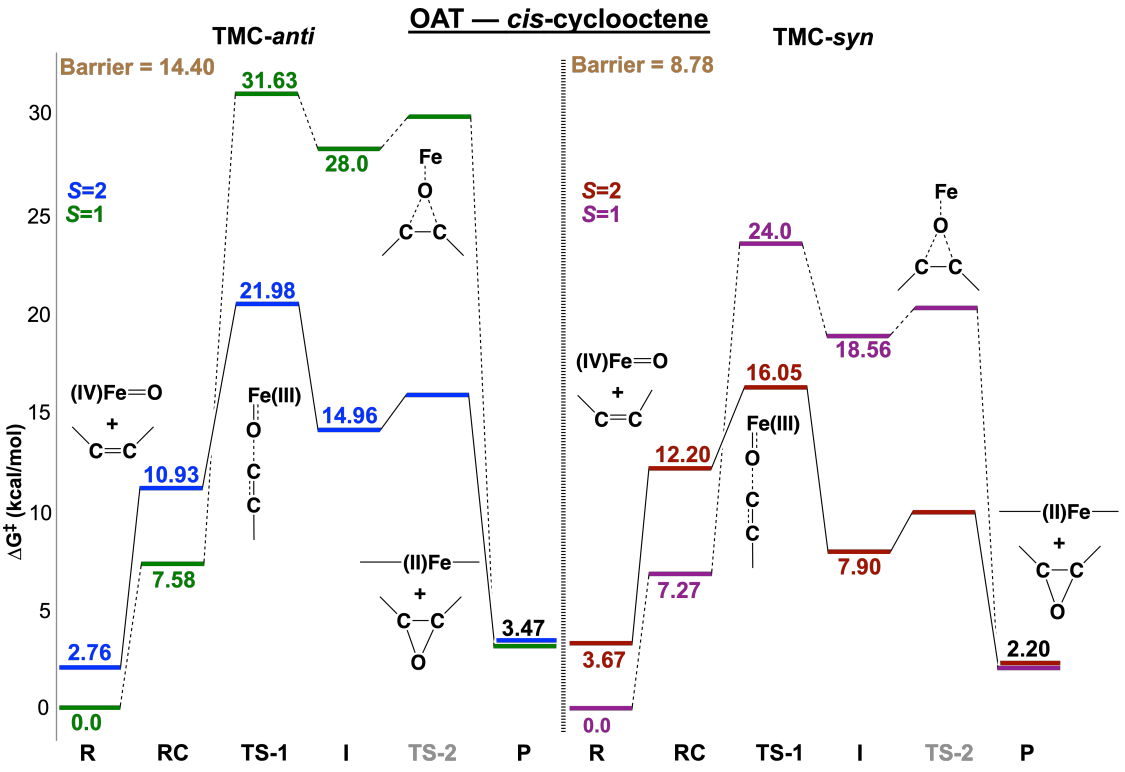

Fig. S21c. Potential Energy Surface for OAT to *cis*-cyclooctene. Where R is the energy of reactants (TMC-*syn/anti* + *cis*-cyclooctene), RC = reactant complex, TS-1 = first transition state, I = intermediate, and P is the energy of products. The transition energy barrier at the top left of each panel represents the $\Delta G^{\ddagger}$ = (TS, *S* = 2) - (RC, *S* = 1).

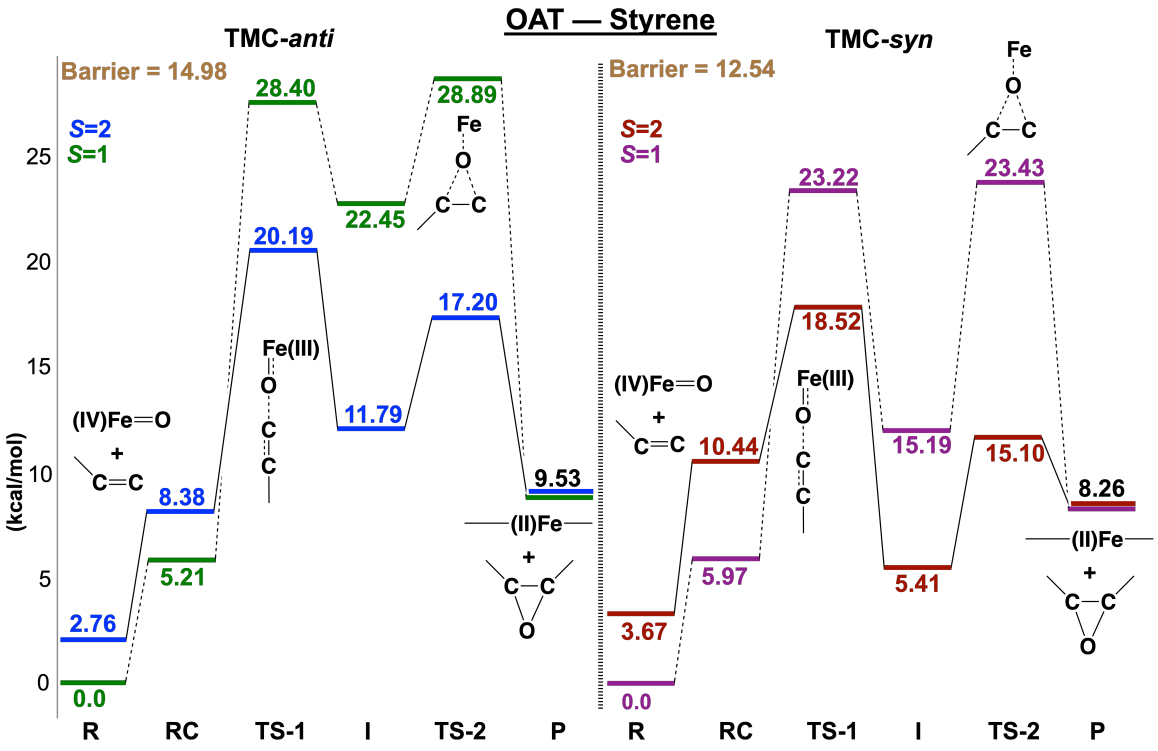

Fig. S21d. Potential Energy Surface for OAT to styrene. Where R is the energy of reactants (TMC-*syn/anti* + *styrene*), RC = reactant complex, TS-1 = first transition state, I = intermediate, TS-2 = second transition state and P is the energy of products. The transition energy barrier at the top left of each panel represents the $\Delta G^{\ddagger}$ = (TS, *S* = 2) - (RC, *S* = 1).

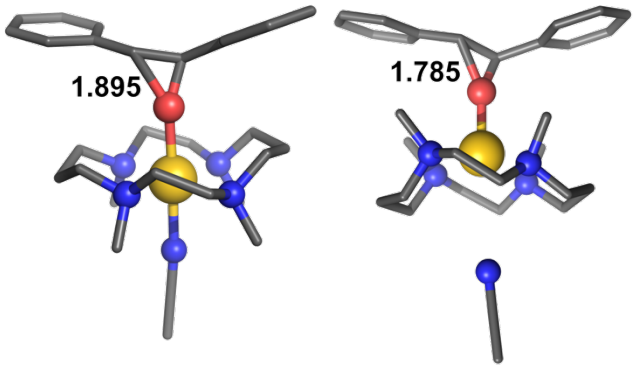

Fig. S22. Bond distances between the O and the proximal C atoms of *trans*-stilbene at the second transition state: 1.895 Å for TMC-*anti* and 1.785 Å for TMC-*syn*.

Table S1. DFT-derived distances of TMC-*anti* and TMC-*syn* complexes

r (Å)	**TMC-*anti*** ***S* = 1**	**TMC-*anti*** ***S* = 2**	**TMC-*syn*** ***S* = 1**	**TMC-*syn*** ***S* = 2**
r(Fe-N4-oop)				
reactants	-0.027	-0.026	+0.106	+0.155
HAT reactions				
TS DHA	-0.018	+0.006	+0.094	+0.219
TS cyclohexene	0.000	+0.011	+0.284	+0.248
OAT reactions				
TS thioanisole	+0.028	+0.068	+0.342	+0.506
TS styrene	+0.029	+0.035	+0.304	+0.270
r(CH_3CN-N4-oop)				
reactants	-2.052	-2.038	-1.981	-1.917
HAT reactions				
TS DHA	-2.031	-2.111	-1.961	-2.049
TS cyclohexene	-2.176	-2.123	-1.987	-2.082
OAT reactions				
TS thioanisole	-2.244	-2.148	-3.243	-3.193
TS styrene	-2.181	-2.118	-2.968	-2.121
r(Fe-NCMe)				
reactants	2.02	2.01	2.09	2.07
HAT reactions				
TS DHA	2.01	2.12	2.05	2.27
TS cyclohexene	2.18	2.13	2.27	2.33
OAT reactions				
TS thioanisole	2.27	2.21	3.59	3.70
TS styrene	2.21	2.15	3.27	2.39

Out-of-plane distances of the Fe=O [*r(Fe-N4-oop)]* and the CH_3CN [*r(CH_3CN-N4-oop)]* units relative to the N4 plane (B97-D3/TZ2P) for *S* = 1 and *S* = 2 states of TMC-*anti* and TMC-*syn*, for Fe=O reactants, and transition states of HAT (DHA, *c*-C_6H_{10}) and OAT (PhSMe, styrene) substrates. Finally, [*r(Fe-NCMe)]* corresponds to relative distance between Fe and nitrogen of axial MeCN.

Table S2. Gibbs energies (B97-D3/TZ2P, COSMO/ZORA) for reaction barriers of OAT to sulfides

$\Delta G^{\ddagger}$ (kcal·mol^{-1})	$\Delta G^{\ddagger}$ = (TS,*S* = 2) - (rev,*S* = 1)	
	TMC-*anti*	TMC-*syn*
MeSMe	13.12	4.44
PhSMe	15.75	4.55
PhSPh	17.59	6.33

Table S3. DFT-derived spin (MDC-m spin) and charges (MDC-d Q) of TMC-*anti* and TMC-*syn* complexes and their differences (*i.e.* spin/charge of TMC-*anti* - spin/charge of TMC-*syn*)

TMC-*anti*	MDC-m spin	MDC-d Q	TMC-*syn*	MDC-m spin	MDC-d Q	Diff. Spin	Diff. Q
-N(CH_2)$_2$N-			**-N(CH_2)$_2$N-**				
H 26	-0.001827	0.00592	H 5	-0.001087	0.010938	-0.00074	-0.005018
H 27	0.001996	-0.020817	H 6	-0.000093	-0.008719	0.002089	-0.012098
H 23	-0.000999	0.01119	H 8	-0.001753	0.015906	0.000754	-0.004716
H 24	0.000218	-0.013689	H 9	0.000127	-0.035011	0.000091	0.021322
H 11	0.000216	-0.013905	H 22	0.000118	-0.035071	0.000098	0.021166
H 12	-0.000983	0.011158	H 23	-0.001753	0.015768	0.00077	-0.00461
H 8	-0.001818	0.006007	H 26	-0.001103	0.010677	-0.000715	-0.00467
H 9	0.001987	-0.021021	H 25	-0.000086	-0.00875	0.002073	-0.012271
-N(CH_2)$_3$N-			**-N(CH_2)$_3$N-**				
H 21	-0.002572	-0.005525	H 13	0.000059	-0.03595	-0.002631	0.030425
H 20	0.002468	-0.029087	H 12	-0.002642	0.003884	0.00511	-0.032971
H 18	0.000447	-0.037611	H 16	0.000101	0.001842	0.000346	-0.039453
H 17	0.000308	0.001796	H 15	-0.00008	-0.037229	0.000388	0.039025
H 14	-0.002556	-0.005582	H 18	0.000063	-0.03546	-0.002619	0.029878
H 15	0.002461	-0.028998	H 19	-0.002632	0.003933	0.005093	-0.032931
H 36	-0.002967	-0.004533	H 30	0.000047	-0.042164	-0.003014	0.037631
H 35	0.001277	-0.021665	H 29	-0.002627	0.00887	0.003904	-0.030535
H 32	0.000486	-0.042677	H 33	0.000055	0.004864	0.000431	-0.047541
H 33	0.000186	0.000338	H 32	0.000029	-0.028508	0.000157	0.028846
H 29	-0.002955	-0.004422	H 35	0.000045	-0.042329	-0.003	0.037907
H 30	0.001285	-0.02152	H 36	-0.002626	0.008704	0.003911	-0.030224
-N-CH_3			**-N-CH_3**				
H 46	-0.002603	0.004825	H 38	-0.002499	-0.007509	-0.000104	0.012334
H 47	-0.000067	-0.033676	H 39	0.001685	-0.023291	-0.001752	-0.010385
H 48	-0.000231	-0.030831	H 40	-0.000124	-0.027551	-0.000107	-0.00328
H 50	-0.002548	0.003893	H 42	-0.002418	-0.01238	-0.00013	0.016273
H 51	-0.000146	-0.031026	H 43	0.000531	-0.023635	-0.000677	-0.007391
H 52	-0.000076	-0.035939	H 44	0.001147	-0.027092	-0.001223	-0.008847
H 38	-0.002547	0.003989	H 46	-0.002413	-0.01228	-0.000134	0.016269
H 39	-0.000083	-0.036231	H 47	0.001156	-0.027395	-0.001239	-0.008836
H 40	-0.000141	-0.030652	H 48	0.000515	-0.02335	-0.000656	-0.007302
H 42	-0.002576	0.004671	H 50	-0.002499	-0.007339	-7.7E-05	0.01201
H 43	-0.000232	-0.03091	H 51	-0.000115	-0.027055	-0.000117	-0.003855
H 44	-0.000061	-0.033881	H 52	0.001696	-0.023512	-0.001757	-0.010369

The numbers assigned to hydrogen atoms are according to the optimized geometry of TMC-*anti* and TMC-*syn*, which can be visualized at DOI: https://doi.org/10.19061/iochem- bd-4-65.

SI References

1. A. D. Cardenal, A. Maity, W.-Y. Gao, R. Ashirov, S.-M. Hyun, D. C. Powers, Iodosylbenzene Coordination Chemistry Relevant to Metal–Organic Framework Catalysis. *Inorg. Chem.* **58**, 10543 (2019)
2. K. S. Hagen, Iron (II) Triflate salts as convenient substitutes for perchlorate salts: Crystal structures of $[Fe(H_2O)_6](CF_3SO_3)_2$ and $Fe(MeCN)_4(CF_3SO_3)_2$. *Inorg. Chem.* **39**, 5867 (2000)
3. J. U. Rohde, J.H. In, M. H. Lim, W. W. Brennessel, M. R. Bukowski, A. Stubna, E. Münck, W. Nam, L. Que, Crystallographic and Spectroscopic Characterization of a Nonheme Fe (IV)=O Complex. *Science*, **299**, 1037-1039 (2003)
4. J. Prakash, G. T. Rohde, K. K. Meier, E. Münck, L. Que Jr., Upside Down! Crystallographic and Spectroscopic Characterization of an $[Fe^{IV}(O_{syn})(TMC)]^{2+}$ Complex. *Inorg. Chem.* **54**, 11055–11057 (2015)
5. E.J. Baerends, T. Ziegler, A.J. Atkins, J. Autschbach, O. Baseggio, D. Bashford, A. Bérces, F.M. Bickelhaupt, C. Bo, P.M. Boerrigter, L. Cavallo, C. Daul, D.P. Chong, D.V. Chulhai, L. Deng, R.M. Dickson, J.M. Dieterich, D.E. Ellis, M. van Faassen, L. Fan, T.H. Fischer, A. Förster, C. Fonseca Guerra, M. Franchini, A. Ghysels, A. Giammona, S.J.A. van Gisbergen, A. Goez, A.W. Götz, J.A. Groeneveld, O.V. Gritsenko, M. Grüning, S. Gusarov, F.E. Harris, P. van den Hoek, Z. Hu, C.R. Jacob, H. Jacobsen, L. Jensen, L. Joubert, J.W. Kaminski, G. van Kessel, C. König, F. Kootstra, A. Kovalenko, M.V. Krykunov, E. van Lenthe, D.A. McCormack, A. Michalak, M. Mitoraj, S.M. Morton, J. Neugebauer, V.P. Nicu, L. Noodleman, V.P. Osinga, S. Patchkovskii, M. Pavanello, C.A. Peeples, P.H.T. Philipsen, D. Post, C.C. Pye, H. Ramanantoanina, P. Ramos, W. Ravenek, J.I. Rodríguez, P. Ros, R. Rüger, P.R.T. Schipper, D. Schlüns, H. van Schoot, G. Schreckenbach, J.S. Seldenthuis, M. Seth, J.G. Snijders, M. Solà, M. Stener, M. Swart, D. Swerhone, V. Tognetti, G. te Velde, P. Vernooijs, L. Versluis, L. Visscher, O. Visser, F. Wang, T.A. Wesolowski, E.M. van Wezenbeek, G. Wiesenekker, S.K. Wolff, T.K. Woo, A.L. Yakovlev, ADF 2019.3, SCM, Theoretical Chemistry, Vrije Universiteit, Amsterdam, The Netherlands (2019)
6. G. te Velde, F. M. Bickelhaupt, E. J. Baerends, C. Fonseca Guerra, S. J. A. van Gisbergen, J. G. Snijders and T. Ziegler, Chemistry with ADF. *J. Comput. Chem.*, **22**, 931–967 (2001)
7. M. Swart and F. M. Bickelhaupt, QUantum-regions Interconnected by Local Descriptions. *J. Comput. Chem.*, **29**, 724–734 (2008)
8. E. van Lenthe and E. J. Baerends, Optimized Slater-type Basis Sets for the Elements 1–118. *J. Comput. Chem.*, **24**, 1142-1156 (2003)
9. D. P. Chong, E. van Lenthe, S. J. A. van Gisbergen and E. J. Baerends, Even-tempered Slater-type Orbitals Revisited: From Hydrogen to Krypton. *J. Comput. Chem.*, **25**, 1030–1036 (2004)
10. S. K. Wolff, Analytical Second Derivatives in the Amsterdam Density Functional Package. *Int. J. Quantum Chem.*, **104**, 645–659 (2005)
11. S. Grimme, J. Antony, S. Ehrlich, H. Krieg, A Consistent and Accurate *ab initio* Parametrization of Density Functional Dispersion Correction (DFT-D) for the 94 Elements H-Pu. *The Journal of Chemical Physics* **132**, 154104 (2010).
12. S. Grimme, Semiempirical GGA-type Density Functional Constructed with a Long-range Dispersion Correction. *J. Comput. Chem.* **27**, 1787–1799 (2006)
13. A. Klamt and G. Schüürmann, COSMO: A New Approach to Dielectric Screening in Solvents with Explicit Expressions for the Screening Energy and its Gradient. *J. Chem. Soc. Perkin Trans. 2*, **5**, 799–805 (1993)
14. M. Swart, E. Rösler and F. M. Bickelhaupt, Proton Affinities in Water of Maingroup-Element Hydrides–Effects of Hydration and Methyl Substitution. *Eur. J. Inorg. Chem.*, **23**, 3646–3654 (2007)

15. B. B. Averkiev and D. G. Truhlar, Free Energy of Reaction by Density Functional Theory: Oxidative Addition of Ammonia by an Iridium Complex with PCP Pincer Ligands. *Catal. Sci. Technol.*, **1**, 1526–1529 (2011)
16. J. E. M. N. Klein, B. Dereli, L. Que Jr. and C. J. Cramer, Why Metal–oxos React with Dihydroanthracene and Cyclohexadiene at Comparable Rates, Despite Having Different C–H Bond Strengths. A Computational Study. *Chem. Commun.*, **52**, 10509–10512 (2016)
17. E. van Lenthe, E. J. Baerends and J. G. Snijders, Relativistic Regular Two-component Hamiltonians. *J. Chem. Phys.*, **99**, 4597–4610 (1993)
18. M. D. Wilkinson, M. Dumontier, I. J. Aalbersberg, G. Appleton, M. Axton, A. Baak, N. Blomberg, J.-W. Boiten, L. B. da Silva Santos, P. E. Bourne, J. Bouwman, A. J. Brookes, T. Clark, M. Crosas, I. Dillo, O. Dumon, S. Edmunds, C. T. Evelo, R. Finkers, A. Gonzalez-Beltran, A. J. G. Gray, P. Groth, C. Goble, J. S. Grethe, J. Heringa, P. A. C. 't Hoen, R. Hooft, T. Kuhn, R. Kok, J. Kok, S. J. Lusher, M. E. Martone, A. Mons, A. L. Packer, B. Persson, P. Rocca-Serra, M. Roos, R. van Schaik, S.-A. Sansone, E. Schultes, T. Sengstag, T. Slater, G. Strawn, M. A. Swertz, M. Thompson, J. van der Lei, E. van Mulligen, J. Velterop, A. Waagmeester, P. Wittenburg, K. Wolstencroft, J. Zhao and B. Mons, *Scientific Data*, **3**, 160018 (2016)
19. S. Matsika, and P. Krause, Nonadiabatic Events and Conical Intersections. Nonadiabatic Events and Conical Intersections. *Annu. Rev. Phys. Chem.* **62**, 621–643 (2011)
20. S. Matsika, & D. R. Yarkony, On the Effects of Spin-orbit Coupling on Conical Intersection Seams in Molecules with an Odd Number of Electrons. I. Locating the Seam. *J. Chem. Phys.* **115**, 2038–2050 (2001)
21. L. Blancafort, Photochemistry and Photophysics at Extended Seams of Conical Intersection. *ChemPhysChem* **15**, 3166–3181 (2014)
22. J. N. Harvey, M. Aschi, H. Schwarz, and W. Koch, The Singlet and Triplet States of Phenyl Cation. A Hybrid Approach for Locating Minimum Energy Crossing Points Between Non-Interacting Potential Energy Surfaces. *Theor. Chem. Acc. Theory Comput. Model. Theor. Chim. Acta* **99**, 95–99 (1998)
23. K.-B. Cho, H. Hirao, S. Shaik, and W. Nam, To Rebound or Dissociate? This is the Mechanistic Question in C–H Hydroxylation by Heme and Nonheme Metal–oxo Complexes. *Chem. Soc. Rev.* **45**, 1197–1210 (2016)
24. M. L. Merlini, G. J. P. Britovsek, M. Swart, and P. Belanzoni, Understanding the Catalase-Like Activity of a Bioinspired Manganese (II) Complex with a Pentadentate NSNSN Ligand Framework. A Computational Insight into the Mechanism. *ACS Catal.* **8**, 2944–2958 (2018)
25. L. D'Amore, L. Belpassi, J. E. M. N. Klein, M. Swart, Spin-resolved charge displacement analysis as an intuitive tool for the evaluation of cPCET and HAT scenarios. *Chem. Commun.* **56**, 12146–12149 (2020).
26. L. Belpassi, I. Infante, F. Tarantelli, L. Visscher, The Chemical Bond between Au(I) and the Noble Gases. Comparative Study of NgAuF and $NgAu^+$ (Ng = Ar, Kr, Xe) by Density Functional and Coupled Cluster Methods. *J. Am. Chem. Soc.* **130**, 1048–1060 (2008).
27. J. E. M. N. Klein, G. Knizia, cPCET versus HAT: A Direct Theoretical Method for Distinguishing X–H Bond-Activation Mechanisms. *Angew Chem Int Ed* **57**, 11913–11917 (2018).
28. Y.-M. Lee, H. Kotani, T. Suenobu, W. Nam, S. Fukuzumi, Fundamental Electron-Transfer Properties of Non-heme Oxoiron(IV) Complexes. *J. Am. Chem. Soc.* **130**, 434–435 (2008).